Fabrication and characterization of rare-earth (Ce, Sm) doped ZnO nanomaterials for use in electronic devices

by

Mustafa Abaas Mohamedelkhair Ahmed

Submitted in partial fulfillment of the requirements for the degree
Doctor of Philosophy (PhD) in Physics
In the Faculty of Natural and Agricultural Sciences
University of Pretoria
Pretoria

Supervisor: Prof. Jackie M Nel

Co-supervisor: Prof. Walter E Meyer

February 2020

Dedication

To my lovely wife Eman Mahgoub, my daughter, Aya Mustafa, my sisters; Anfal Abaas and Isra Abaas
for their love, support and prayers for my success
&
To my lovely parents,
for their encouragement and support during the entire journey of education and putting me through the best education

Declaration

I, Mustafa Abaas Mohamedelkhair Ahmed declare that the thesis, which I hereby submit for the degree Doctor of Philosophy (PhD) in Physics at the University of Pretoria, is my own work and has not previously been submitted by me for a degree at this or any other tertiary institution.

Signature .....

Date .....

Acknowledgements

All praise goes to Almighty **ALLAH**, the creator and the sustainer of the whole universe, for granting me the strength and the abilities to complete this PhD.

For the success of my PhD study, I would like to express and extend my acknowledgement to the following people:

- My supervisor, Professor Jackie M Nel and my co-supervisor, Professor Walter E Meyer for their support, guidance and discussions through the entire period of this study.
- Doctor Malven Shandirai and Helga Danga for their help in depositing contacts with thermal evaporation system during the earlier stage of my PhD.
- Mr. Johan Janse van Rensburg and Mr Matshisa Legodi for helping with temperature dependent *I-V* and *C-V* set up as well as discussion and support during the period of my PhD.
- Doctor. Bernard Mwankemwa, for his support and discussion during my study.
- Professor Ted Kroon and Professor Hendrik Swart from the University of the Free State for their help with PL and XRD measurements.
- Professor Danie Auret for his discussions and guidance during the course of the study.
- Professor Shankara Radhakrishnan at the Chemistry Department for the UV-vis measurements.
- I would like to express thanks to all members of the Electronic Material and Thin Films Group.
- I would also like to thank the Head of Physics Department, Professor Chris Theron, for allowing me to my PhD at this wonderful department.
- Special thank goes to the University of Khartoum and Ministry of Higher Education and scientific research for funding my study.
- I would also like to thank the University of Pretoria for financial assistance.
- I want to thank my parents and my sisters, Isra and Anfal for their love, support, encouragement and contentious prayers to complete this PhD.
- Last but not least, I would also thank my wife Eman Mahgoub and my sweet daughter, Aya Mustafa for their support and sacrifices during the course of my PhD.

Abstract

The aim of the study is to synthesize and characterize high quality undoped, Ce doped, Sm doped, Ce and Sm co-doped, and Ce and Al co-doped ZnO thin films and nanorods for use in optoelectronic devices, using the low-cost sol-gel and chemical bath deposition techniques.

Undoped, Ce doped (up to 2.0 at.%), Sm doped (up to 2.0 at.%), Ce and Sm co-doped (up to 2.0 at.% each), and Ce and Al co-doped (up to 7.0 at.% Ce and 1.0 at.% Al) ZnO thin films on glass and n-Si substrates were investigated. X-ray diffraction revealed the incorporation of the dopant into the ZnO lattice, with the exception of the highly doped Ce and Al co-doped sample, where the lattice parameters decreased and CeO_2 was observed. Doping increased the lattice parameter and, at low concentration (2.0 at.% or less), improved crystalinity, but not at higher doping concentration. Room temperature photoluminescence spectroscopy revealed both UV and visible light emission from the Ce and Al co-doped samples, while for the other films only a peak in the UV (at 400 nm) was observed. The visible light emission was at 450 - 850 nm and was attributed to defect formation. Schottky diodes fabricated on the films deposited on n-Si showed good rectification behaviour for all films. The ZnO films co-doped with Ce and Sm manifested excellent rectification of six orders of magnitude, a barrier height of 0.82 eV, ideality factor of 1.62 and series resistance of 60 Ω.

ZnO nanorods that were grown as un-doped, Sm doped (up to 5.5 at.%), Ce doped (up to 10 at.%), Ce and Sm co-doped (up to 0.8 at.%) were grown by means of chemical bath deposition on glass, ITO-coated glass and n-Si substrates that were seeded with ZnO by sol-gel spin coating. X-ray diffraction revealed the incorporation of the dopants into the ZnO lattice. In all cases doping increased the lattice parameter and improved crystalinity. Raman spectroscopy showed the characteristic E_2 (high) mode peak was the prominent and its position shifted towards a lower wave number after doping. For all samples, the photoluminescence showed peaks in both the UV and visible (450 - 800 nm) region. Schottky diodes fabricated on the nanorods deposited on both the ITO-coated glass substrates and the n-Si substrate showed good rectification. The 1.5 at.% Sm doped ZnO on ITO had an ideality factor of 2.5 and barrier height of 0.72 eV, while the 10.0 at.% Ce doped ZnO on ITO had the lowest ideality factor of 1.34, Schottky barrier height of 0.856 eV and series resistance of 130 Ω. The *I-V* characteristics of the Ce and Sm co-doped nanorods grown on n-Si showed an increase in the generation-recombination current with increasing dopant concentration. The current transport mechanism in the diode was dominated by approximately ohmic leakage conduction mechanism at a

lower voltage (0.0 to 0.6 V), while at a voltage higher than 0.6 V, the space-charge limited current and the trap-filled limit voltage mechanism dominated.

Table of contents

Chapter 1

Introduction

1.1 Background and motivation

Zinc oxide semiconductor material has a wide and direct band gap with a band gap energy of 3.37 eV, and large exciton binding energy (60 meV) at room temperature, and has been the subject of interest in recent years, especially in its nanostructure form [1]. Its large exciton binding energy, compared to its counterpart GaN (25 meV), makes ZnO promising candidate for blue and ultra-violet lasers and LEDs [2]. Also, undoped ZnO has a high electron mobility (137 cm^2/Vs), good transparency and high thermal conductivity (98 - 116 W/mK). Moreover, its large band gap makes it a good material for photonic applications in the blue and UV spectral range [3]. Besides tin oxide and indium oxide, ZnO is considered as a member of transparent conducting oxides (TCO). Generally, TCOs are used in a wide range of applications such as solar cells and display devices due to their low resistivity, high transparency and chemical stability [4]. Apart from these excellent properties, indium tin oxide (ITO) is costly and indium is scarce [5]. Therefore, ZnO is considered as a good candidate to replace ITO due to its previously mentioned properties. Furthermore, ZnO appears naturally as an n-type material, where the native point defects such as oxygen vacancies and Zn interstitials are responsible for its conductivity. The presence of these defects makes it difficult to produce p-type ZnO. However, doping of ZnO with some metals and metal-N combinations such as Ga-N [6], Sb [7], N-Al [8] and Li [9, 10] has resulted in p-type conductivity in ZnO. The presence of such native defects in ZnO has also inhibited the fabrication of UV light emitting diodes due to their self-compensation [1].

ZnO nanostructured materials such as zero-dimensional, one dimensional and two dimensional structures can be reproducibly synthesized and investigated for different applications in nano-devices. These low dimensional structures are the basic building blocks for technologies nowadays due to their interesting and unique properties in device applications at the nanoscale [11–15]. For example, one-dimensional nanorods based on various materials such as Si, GaN and ZnO have been successfully prepared and reported in the literature [16–18]. Among these nanostructured materials, ZnO is a

promising candidate in electronic applications owing to its easy formation of nanostructures, low temperature growth [19], non-toxicity and the higher availability of Zn compared to Ga and In [20]. Its resistance to high energy radiation in comparison with GaN, makes it suitable for space and nuclear applications [21–23]. In addition, by adopting various growth techniques, different morphologies of ZnO have been fabricated and used in a wide range of applications such as light emitting diodes (LEDs) [24], optical waveguides [25, 26] chemical and gas sensors [27, 28], solar cells [29, 30], laser diodes [31], UV-light emitters [32, 33] and UV-photodiodes [34, 35]. Moreover, ZnO nanostructures have been used in Schottky diode device applications [36–39].

In the recent years, ZnO properties have been explored by doping it with metals such as Ag [40], Ga [41], Mg [42], Al [43] and Mn [44]. Also, rare-earth (RE) ions are used substantially as activators owing to their narrow fluorescence band and high fluorescence efficiencies. These dopants include, Yb [45], Eu [46], La [47], Er [48], Gd [49], Ce [50] and Sm [51]. Among these, Ce and Sm doped ZnO has shown good optical and electrical properties. Yousefi *et al.* [52] found that Ce doping of ZnO enhanced the photoresponsivity. Narayanan and co-workers [53] found enhancement in the photocatalytic efficiency and a decrease in the electrical resistivity in Ce doped ZnO thin films grown by spray pyrolysis. Moreover, Ce has unique properties, such as the redox couple properties that allows the cerium oxidation to shift between Ce_2O_3 and CeO_2 under certain conditions, the easy formation of O vacancies and control over modifying the morphological properties of the host [54]. On the other hand Sm doped ZnO has gained much interest owing to a number of advantages, such as improving the electrical, magnetic and optical properties, as well as the scintillation, luminescence, oxygen gain and surface roughness compared to widely used Al, which is reported only to improve the electrical properties and decrease the optical transmittance of ZnO [55]. Furthermore, Sm doping of ZnO thin films has been found to enhance the green emission [56].

Some of the methods used to prepare these films are expensive, sophisticated techniques, requiring high vacuum and high temperature processes. Therefore, in this work, low temperature, inexpensive sol-gel and chemical bath deposition (CBD) methods were adopted to synthesize the ZnO thin films and nanorods.

1.2 Aims and objectives

The aim of the study is to fabricate and characterize Schottky diode devices based on Ce, Sm and Al doped and co-doped ZnO thin films and nanorods using low cost and low temperature sol-gel and CBD methods for use in optoelectronic devices. The objectives are listed as follows:

1. To synthesize high quality undoped and Ce, Sm and Al doped and co-doped ZnO thin films by low-cost sol-gel technologies and study their structural, morphological and optical properties.

2. To investigate the electrical properties of the fabricated Schottky diode devices based on undoped and Ce, Sm and Al doped and co-doped ZnO thin films using *I-V* characteristics.

3. To fabricate and characterize undoped and Sm-doped ZnO nanorods on ITO substrates and to study their microstructure, morphology and optical properties, as well as their Schottky diode properties by using *I-V* characteristics.

4. To synthesize and characterize high quality nanorods based on undoped and Ce-doped ZnO, and study their structural and optical properties.

5. To investigate the effect of Sm doping of ZnO nanorods on the electrical properties of the Schottky diode by employing *I-V* characteristics.

6. To fabricate high quality undoped and Ce, Sm co-doped ZnO nanorods on an n-Si substrate by employing CBD and study their structural, morphological, and optical properties.

7. To investigate the effect of Ce, Sm co-doping on the Schottky diode properties using *I-V* characteristics.

1.3 Structure of the thesis

The thesis is presented in seven (7) chapters:

Chapter 1 gives an introduction to and motivation for the thesis, aims and objectives, as well as the organization of the thesis.

Chapter 2 gives literature review on ZnO as semiconductor, including the theory of the sol-gel and chemical bath methods used to synthesis the ZnO thin films and nanorods, respectively.

Chapter 3 summarises the theoretical background of metal semiconductor contacts.

Chapter 4 describes the experimental procedures and the growth techniques used to synthesize the samples and to fabricate the ohmic and Schottky contacts. A brief explanation of the characterization techniques employed in this study is also given.

Chapter 5 presents and discusses the results obtained from undoped and Ce, Sm and Al doped and co-doped ZnO thin films grown by sol-gel spin coating.

Chapter 6 presents and discusses the results obtained from the ZnO nanorods based on undoped, Ce and Sm doped and co-doped ZnO nanorods by using low temperature CBD.

Chapter 7 summarises conclusions drawn from this study and expands on future work to be done.

References

[1] M. Willander, O. Nur, Q. Zhao, L. Yang, M. Lorenz, B. Cao, J. Z. Pérez, C. Czekalla, G. Zimmermann, M. Grundmann, Zinc oxide nanorod based photonic devices: recent progress in growth, light emitting diodes and lasers, Nanotechn. 20 (33) (2009) 332001.

[2] J. Lim, C. Kang, K. Kim, I. Park, D. Hwang, S. Park, UV electroluminescence emission from ZnO light-emitting diodes grown by high-temperature radiofrequency sputtering, Adv. Mater. 18 (20) (2006) 2720–2724.

[3] A. Tsukazaki, M. Kubota, A. Ohtomo, T. Onuma, K. Ohtani, H. Ohno, S. F. Chichibu, M. Kawasaki, Blue light-emitting diode based on ZnO, Jpn. J. Appl. Phys. 44 (5L) (2005) L643.

[4] M. Yilmaz, Z. Caldiran, A. Deniz, S. Aydogan, R. Gunturkun, A. Turut, Preparation and characterization of sol–gel-derived n-ZnO thin film for Schottky diode application, Appl. Phys. A 119 (2) (2015) 547–552.

[5] S. Okuda, T. Matsuo, H. Chiba, T. Mori, K. Washio, Conductive and transparent V-doped ZnO thin films grown by radio frequency magnetron sputtering, Thin Solid Films 557 (2014) 197–202.

[6] M. Joseph, H. Tabata, T. Kawai, p-type electrical conduction in ZnO thin films by Ga and N codoping, Jpn. J. Appl. Phys. 38 (11A) (1999) L1205.

[7] F. Xiu, Z. Yang, L. Mandalapu, D. Zhao, J. Liu, W. Beyermann, High-mobility Sb-doped p-type ZnO by molecular-beam epitaxy, Appl. Phys. Lett. 87 (15) (2005) 152101.

[8] J. Lu, Z. Ye, F. Zhuge, Y. Zeng, B. Zhao, L. Zhu, p-type conduction in N–Al co-doped ZnO thin films, Appl. Phys. Lett. 85 (15) (2004) 3134–3135.

[9] M. Wardle, J. Goss, P. Briddon, Theory of Li in ZnO: A limitation for Li-based p-type doping, Phys. Rev. B 71 (15) (2005) 155205.

[10] Y. Zeng, Z. Ye, W. Xu, D. Li, J. Lu, L. Zhu, B. Zhao, Dopant source choice for formation of p-type ZnO: Li acceptor, Appl. Phys. Lett. 88 (6) (2006) 062107.

[11] Y. Xia, P. Yang, Y. Sun, Y. Wu, B. Mayers, B. Gates, Y. Yin, F. Kim, H. Yan, One-dimensional nanostructures: synthesis, characterization, and applications, Adv. Mater. 15 (5) (2003) 353–389.

[12] L. Samuelson, C. Thelander, M. Björk, M. Borgström, K. Deppert, K. Dick, A. Hansen, T. Mårtensson, N. Panev, A. Persson, Semiconductor nanowires for 0D and 1D physics and applications, Physica E: Low Dimens. Syst. Nanostruct. 25 (2-3) (2004) 313–318.

[13] H. Tian, J. Tice, R. Fei, V. Tran, X. Yan, L. Yang, H. Wang, Low-symmetry two-dimensional materials for electronic and photonic applications, Nano Today 11 (6) (2016) 763–777.

[14] A. H. Khan, S. Ghosh, B. Pradhan, A. Dalui, L. Shrestha, S. Acharya, K. Ariga, Two-dimensional 2D nanomaterials towards electrochemical nanoarchitectonics in energy-related applications, Bull. Chem. Soc. Jpn. 90 (6) (2017) 627–648.

[15] Y. Yang, H. Du, Q. Xue, X. Wei, Z. Yang, C. Xu, D. Lin, W. Jie, J. Hao, Three-terminal memtransistors based on two-dimensional layered gallium selenide nanosheets for potential low-power electronics applications, Nano Energy 57 (2019) 566–573.

[16] K. Peng, Y. Xu, Y. Wu, Y. Yan, S. Lee, J. Zhu, Aligned single-crystalline Si nanowire arrays for photovoltaic applications, Small 1 (11) (2005) 1062–1067.

[17] J. Xiang, W. Lu, Y. Hu, Y. Wu, H. Yan, C. M. Lieber, Ge/Si nanowire heterostructures as high-performance field-effect transistors, Nat. 441 (7092) (2006) 489.

[18] L. Vayssieres, Growth of arrayed nanorods and nanowires of ZnO from aqueous solutions, Adv. Mater. 15 (5) (2003) 464–466.

[19] V. Kabra, L. Aamir, M. Malik, Low cost, p-ZnO/n-Si , rectifying, nano heterojunction diode: Fabrication and electrical characterization, Beilstein J. Nanotechnol. 5 (2014) 2216.

[20] L. J. Brillson, Y. Lu, ZnO Schottky barriers and ohmic contacts, J. Appl. Phys. 109 (12) (2011) 8.

[21] D. C. Look, D. Reynolds, J. W. Hemsky, R. Jones, J. Sizelove, Production and annealing of electron irradiation damage in ZnO, Appl. Phys. Lett. 75 (6) (1999) 811–813.

[22] A. Polyakov, N. Smirnov, A. Govorkov, E. Kozhukhova, V. Vdovin, K. Ip, M. Overberg, Y. Heo, D. Norton, S. Pearton, Proton implantation effects on electrical and recombination properties of undoped ZnO, J. Appl. Phys. 94 (5) (2003) 2895–2900.

[23] F. Tuomisto, K. Saarinen, D. C. Look, G. C. Farlow, Introduction and recovery of point defects in electron-irradiated ZnO, Phys. Rev. B. 72 (8) (2005) 085206.

[24] W. Xu, Z. Ye, Y. Zeng, L. Zhu, B. Zhao, L. Jiang, J. Lu, H. He, S. Zhang, ZnO light-emitting diode grown by plasma-assisted metal organic chemical vapor deposition, Appl. Phys. Lett. 88 (17) (2006) 173506.

[25] H. Baek, H. Kwak, M. S. Song, G. E. Ha, J. Park, Y. Tchoe, J. K. Hyun, H. Y. Park, E. Cheong, G. Yi, ZnO nanotube waveguide arrays on graphene films for local optical excitation on biological cells, Appl. Mater. 5 (4) (2017) 046106.

References

[26] O. Jamadi, F. Reveret, P. Disseix, F. Medard, J. Leymarie, A. Moreau, D. Solnyshkov, C. Deparis, M. Leroux, E. Cambril, et al., Edge-emitting polariton laser and amplifier based on a ZnO waveguide, Light Sci. Appl. 7 (1) (2018) 82.

[27] R. Ahmad, N. Tripathy, M. Ahn, Y. Hahn, Highly stable hydrazine chemical sensor based on vertically-aligned ZnO nanorods grown on electrode, J. Colloid Interface Sci. 494 (2017) 153–158.

[28] A. Umar, M. Rahman, Y. Hahn, Ultra-sensitive hydrazine chemical sensor based on high-aspect-ratio ZnO nanowires, Talanta 77 (4) (2009) 1376–1380.

[29] M. Patel, H. Kim, J. Kim, J. Yun, S. Kim, E. Choi, H. Park, Excitonic metal oxide heterojunction (NiO/ZnO) solar cells for all-transparent module integration, Sol. Energy Mater. Sol. Cells 170 (2017) 246–253.

[30] X. Dong, D. Chen, J. Zhou, Y. Zheng, X. Tao, High crystallization of a multiple cation perovskite absorber for low-temperature stable ZnO solar cells with high-efficiency of over 20%, Nanoscale. 10 (15) (2018) 7218–7227.

[31] S. Chu, M. Olmedo, Z. Yang, J. Kong, J. Liu, Electrically pumped ultraviolet ZnO diode lasers on Si, Appl. Phys. Lett. 93 (18) (2008) 181106.

[32] X. Fang, Y. Bando, U. Gautam, T. Zhai, H. Zeng, X. Xu, M. Liao, D. Golberg, ZnO and ZnS nanostructures: ultraviolet-light emitters, lasers, and sensors, Crit. Rev. Solid State Mater. Sci. 34 (3-4) (2009) 190–223.

[33] F. Qin, C. Xu, Q. Zhu, J. Lu, D. You, W. Xu, Z. Zhu, A. Manohari, F. Chen, Extra green light induced ZnO ultraviolet lasing enhancement assisted by Au surface plasmons, Nanoscale 10 (2) (2018) 623–627.

[34] S. Liang, H. Sheng, Y. Liu, Z. Huo, Y. Lu, H. Shen, ZnO Schottky ultraviolet photodetectors, J. Cryst. Growth 225 (2-4) (2001) 110–113.

[35] N. Al-Hardan, A. Jalar, M. Hamid, L. Keng, N. Ahmed, R. Shamsudin, A wide-band UV photodiode based on n-ZnO/p-Si heterojunctions, Sensors Actuat. A Phys. 207 (2014) 61–66.

[36] G. Yi, C. Wang, W. Park, ZnO nanorods: synthesis, characterization and applications, Semicond. Sci. Technol. 20 (4) (2005) S22.

[37] F. Yakuphanoglu, Electrical characterization and device characterization of ZnO microring shaped films by sol–gel method, J. Alloy Compd. 507 (1) (2010) 184–189.

[38] L. Wen, K. Wong, Y. Fang, M. Wu, Y. Lei, Fabrication and characterization of well-aligned, high density ZnO nanowire arrays and their realizations in Schottky device applications using a two-step approach, J. Mater. Chem. 21 (20) (2011) 7090–7097.

[39] K. Kim, K. M. Sim, S. Yoon, M. S. Jang, D. S. Chung, Defect Restoration of Low-temperature Sol-Gel-Derived ZnO via Sulfur Doping for Advancing Polymeric Schottky Photodiodes, Adv. Funct. Mater. 28 (30) (2018) 1802582.

[40] Y. Li, X. Zhao, W. Fan, Structural, electronic, and optical properties of Ag-doped ZnO nanowires: first principles study, J. Phys. Chem. C 115 (9) (2011) 3552–3557.

[41] V. Bhosle, A. Tiwari, J. Narayan, Electrical properties of transparent and conducting Ga doped ZnO, J.Appl. Phys. 100 (3) (2006) 033713.

[42] F. Shan, B. Kim, G. Liu, Z. Liu, J. Sohn, W. Lee, B. Shin, Y. Yu, Blueshift of near band edge emission in Mg doped ZnO thin films and aging, J. Appl. Phys. 95 (9) (2004) 4772–4776.

[43] P. Sahay, R. Nath, Al-doped ZnO thin films as methanol sensors, Sensor Actuat. B Chem. 134 (2) (2008) 654–659.

[44] T. Fukumura, Z. Jin, M. Kawasaki, T. Shono, T. Hasegawa, S. Koshihara, H. Koinuma, Magnetic properties of Mn-doped ZnO, Appl. Phys. Lett. 78 (7) (2001) 958–960.

[45] I. Soumahoro, G. Schmerber, A. Douayar, S. Colis, M. Abd-Lefdil, N. Hassanain, A. Berrada, D. Muller, A. Slaoui, H. Rinnert, et al., Structural, optical, and electrical properties of Yb-doped ZnO thin films prepared by spray pyrolysis method, J. Appl. Phys. 109 (3) (2011) 033708.

[46] A. Ishizumi, Y. Kanemitsu, Structural and luminescence properties of Eu-doped ZnO nanorods fabricated by a microemulsion method, Appl. Phys. Lett. 86 (25) (2005) 253106.

[47] T. Jia, W. Wang, F. Long, Z. Fu, H. Wang, Q. Zhang, Fabrication, characterization and photocatalytic activity of La-doped ZnO nanowires, J. Alloy Compd. 484 (1-2) (2009) 410–415.

[48] T. Williams, D. Hunter, A. Pradhan, I. Kityk, Photoinduced piezo-optical effect in Er doped ZnO films, Appl. Phys. Lett. 89 (4) (2006) 043116.

[49] A. Dakhel, M. El-Hilo, Ferromagnetic nanocrystalline Gd-doped ZnO powder synthesized by coprecipitation, J. Appl. Phys. 107 (12) (2010) 123905.

[50] C. Ge, C. Xie, S. Cai, Preparation and gas-sensing properties of Ce-doped ZnO thin-film sensors by dip-coating, Mater. Sci. Eng. B 137 (1-3) (2007) 53–58.

[51] J. Sin, S. Lam, K. Lee, A. R. Mohamed, Preparation and photocatalytic properties of visible light-driven samarium-doped ZnO nanorods, Ceram. Int. 39 (5) (2013) 5833–5843.

[52] M. Yousefi, M. Amiri, R. Azimirad, A. Z. Moshfegh, Enhanced photoelectrochemical activity of Ce doped ZnO nanocomposite thin films under visible light, J. Electroanal. Chem. 661 (1) (2011) 106–112.

References

[53] N. Narayanan, N. Deepak, Realizing luminescent downshifting in ZnO thin films by Ce doping with enhancement of photocatalytic activity, Solid State Sci. 78 (2018) 144–155.

[54] A. J. Kulandaisamy, V. Elavalagan, P. Shankar, G. K. Mani, K. J. Babu, J. B. B. Rayappan, Nanostructured cerium-doped ZnO thin film–A breath sensor, Ceram. Int. 42 (16) (2016) 18289–18295.

[55] Z. B. Ayadi, L. El Mir, K. Djessas, S. Alaya, Electrical and optical properties of aluminum-doped zinc oxide sputtered from an aerogel nanopowder target, Nanotechnology 18 (44) (2007) 445702.

[56] T. Tsuji, Y. Terai, M. Hakim, M. Kawabata, Y. Fujiwara, Photoluminescence properties of Sm-doped ZnO grown by sputtering-assisted metalorganic chemical vapor deposition, J. Non Cryst. Solids 358 (17) (2012) 2443–2445.

Chapter 2

ZnO as semiconductor

2.1 Introduction

Zinc oxide (ZnO) is a binary group II-VI semiconductor with a wide, direct band gap (3.37 eV) at room temperature and large exciton binding energy (60 meV) compared to its GaN counterpart with band gap (3.40 eV) and exciton binding energy of 25 meV [1]. Due to the large exciton binding energy, ZnO has been considered as a good candidate in excitonic emission devices. ZnO has attracted great interest from the research community due to its use in a variety of applications, such as optical waveguides [2], piezoelectric transducers [3], transparent conductive oxides [4], chemical gas sensors [5, 6], UV-light emitters [7] and Schottky diode devices [8–10]. ZnO is also used in biomedical applications [11]. ZnO also has some beneficial electronic properties such as a high electron saturation velocity and a high breakdown voltage compared to Si and GaAs. Moreover, engineering of the ZnO band gap for optoelectronic properties has been done by alloying it with MgO (band gap of 7.8 eV) and CdO (band gap of 2.7 eV) to increase and decrease its band gap, respectively [12]. Furthermore, ZnO normally appears as an n-type semiconductor; however, some research reported p-type conductivity by doping [13–15]. It is chemically stable, environmentally friendly and is easy to prepare in different morphologies at low temperatures. Recently, numerous reports on the growth of bulk and nanostructured ZnO with different morphologies have been published.

2.1.1 Crystal and band structure of ZnO

ZnO as binary compound crystallizes in either hexagonal wurtzite (*B4*), cubic zinc-blende (*B3*) or rock salt (*B1*) structure, where each Zn is surrounded by four oxygen atoms at the corners of a tetrahedron. Figure 2.1 shows the most thermodynamically stable phase at ambient conditions, the wurtzite structure. The other two phases of the ZnO can be grown under specific conditions, for example, the zinc blende structure can be stabilized if growing on a cubic substrate, while the rock

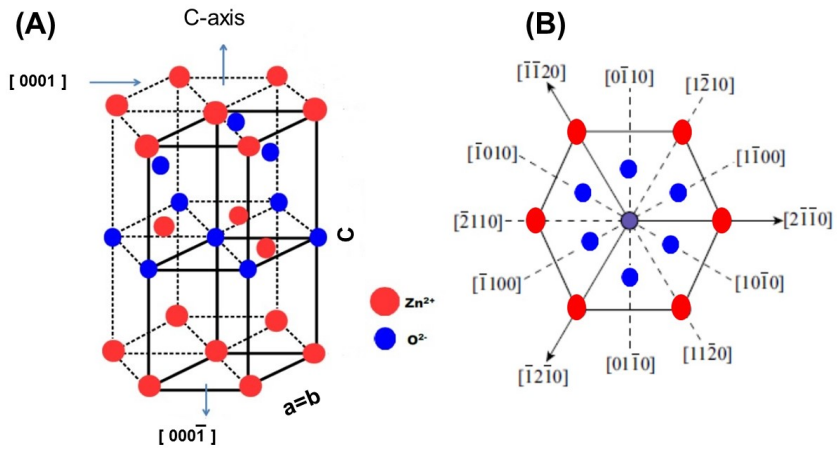

Fig. 2.1 (A) The unit cell of the ZnO wurtzite structure. (B) Different crystal planes orientation of ZnO wurtzite structure. Redrawn from Ref [16].

salt (NaCl) structure can be obtained at high pressure [1]. The lattice parameters of the wurtzite hexagonal structure are $a = 3.250$ Åand $c = 5.207$ Å, and the structure corresponds to the $P6_3mc$ space group with two interconnecting hexagonally close packed (hcp) O^{2-} and Zn^{2+} involving sp^3 covalent bonding [16]. ZnO is an ionic compound that exhibits different surface orientations, as illustrated in Figure 2.1(B). Zn^{2+} and O^{2-} atoms create polar surface along the hexagonal plane that are responsible for the ZnO crystal growth and morphologies such as nanorods, nanotubes, nanowires, nanobelts, nanocubes and nanospheres etc. [17].

The arrangement of the tetrahedral structure of ZnO gives rise to the symmetry of the polar surface along the hexagonal axis. The most common polar surfaces for the wurtzite ZnO structure are [0001] and [000$\bar{1}$], which are terminated by Zn^{2+} or O^{2+} polar faces, respectively, along the c-axis (see Figure 2.1 (A)). These polar surfaces are responsible for the growth orientation, piezoelectricity, defect generation, etching as well as spontaneous polarization of the ZnO. The most common face terminations are the polar Zn terminated (0001) and O terminated (000$\bar{1}$) faces. The non-polar surface (11$\bar{2}$0) and (10$\bar{1}$0) faces that are along the a-axis, accommodate an equal number of O and Zn atoms [18]. The polar faces posses different chemical and physical properties, while the O-terminated faces posses a slightly different electronic structure compared to the other three faces [18]. The unit cell of the ZnO wurtzite structure and its different crystal planes surface orientations are shown in Figure 2.1 (A) and (B), respectively.

The band structure is an important property in semiconductors, since it accounts for the electrical and optical properties observed in different materials. The band structure of a material can be determined theoretically using density functional theory (DFT), or experimentally using ultraviolet (UV) induced photoemission spectroscopy, conventional x-ray and angular photoemission spectroscopy.

Qualitative agreement between theory and experimental results suggests that ZnO is a direct band gap semiconductor [19].

2.2 Growth techniques for ZnO

Nanostructured ZnO can be obtained using physical and chemical methods. These include vapour liquid-solid [20], radio-frequency magnetron sputtering [21], pulsed laser deposition [22], epitaxial electrodeposition [23], metal organic chemical vapour deposition [24], chemical vapour deposition [25], spray pyrolysis [26], sol-gel spin coating [27] and CBD [28]. However, only sol-gel and CBD methods are adopted in this study, as will be outlined in the coming subsections.

2.2.1 Sol-gel

The sol-gel process is a low-cost, effective method that has been used extensively to prepare thin films and nano-particle materials. Briefly, in the sol-gel method the reagent undergoes a transition in a few steps from a liquid (colloidal) to a solid sol. These steps include hydrolysis, condensation, and finally drying process [29]. This method has advantages such as low temperature formation of the gel, ease of casting a complex shape, use of compounds that produce material with no impurities, ability to deposit on a large area on the substrate and inexpensive equipment. The sol-gel method can be divided into an aqueous sol-gel and non-aqueous sol-gel method according to the nature of the solvent being used. In the first case, the reaction medium used is water, while in the latter case, an organic solvent such as alcohols (e.g. ethanol) [29] is used as a reaction medium.

In the aqueous sol-gel process the precursors are nitrates, metal acetates, chlorides, sulphates or metal alkoxides. The oxygen source in this method for the formation of metal-oxide is the water. The disadvantage of this method is the difficulty in controlling the particle morphology [30]. It is highly recommended for bulk metal oxide synthesis and not suitable for nanoscale synthesis. In the non-aqueous sol-gel method, the source of the oxygen needed for the metal oxide formation is the solvent, for examples alcohol, aketones, aldehydes or even the metal precursors [29]. Unlike the aqueous method, it is ease to control and tune the surface properties, size of the particles and also the composition of the final product. Furthermore, this method also allows control of the growth of the nano-particles and avoids their agglomeration. Therefore, it is suitable for the synthesis of nanoscale metal oxide materials [29]. After the formation of the gel, different methods can be used to deposit the sol on the substrate, such as a dip or spin coating. In this study, the non-aqueous sol-gel method and spin coating were employed to deposit the films on glass and Si substrates. More information about the sol-gel process can be found in [31].

2.2.2 Chemical bath deposition

Chemical bath deposition (CBD) is a well-established technique used in the synthesis of ZnO nanorods using an aqueous solution as precursor. CBD is also known as hydrothermal growth; it is a low cost and scalable method for fabrication of high quality ZnO nanorods. It is a low temperature growth technique (60° – 90° C), with simple method, easy formation of the nanorods as well as the nanorod shapes [32]. Deposition of the nanorods using this method can be done on a variety of substrates such as plastic, glass, silicon and polymers. Before the deposition of the nanorods, a ZnO seed (nucleation) layer is deposited on the substrates, using the spin-coating technique. ZnO nanorods are usually prepared from an aqueous solution, when adopting the CBD method, containing hexamethylenetetramine $(CH_2)_6N_4$ as reducing agent and zinc nitrate $Zn((NO_3))_2.6H_2O$. The $Zn(NO_3)_2$ supplies the Zn^{2+} ions while the $(CH_2)_6N_4$ acts as an agent (pH-buffer) that provides the OH^- ions that are needed for the formation of ZnO [33]. The growth mechanisms for growing ZnO nanorods can be described by the following equations [33]:

$$(CH_2)_6N_4 + 6H_2O \longleftarrow 4NH_3 + 6HCH_2O \tag{2.1}$$

$$NH_3 + H_2O \longleftrightarrow NH_4^+ + OH^- \tag{2.2}$$

$$Zn^{2+} + 4OH^- \longleftrightarrow Zn([OH])_4^{-2} \tag{2.3}$$

$$Zn^{2+} + 4NH_3 \longleftrightarrow (Zn[NH_3]_4^{2+}) \tag{2.4}$$

$$(Zn[NH_3]_4^{2+}) + 2OH^{-1} \longrightarrow Zn(OH)_2(NH_3)_4 \tag{2.5}$$

$$Zn([OH])_4^{-2} \longleftarrow Zn(OH)_2 + 2OH^{-1} \tag{2.6}$$

$$Zn[OH]_2 \longrightarrow ZnO + H_2O \tag{2.7}$$

By immersing the seeded substrates into the solution of zinc nitrate and hexamethylenetetramine vertically aligned arrays of nanorods can be produced. The morphologies and the direction of the ZnO nanorods can be varied by controlling the growth parameters such as seed layer, temperature, pH, time and substrate orientation, as well as the molar concentration of the precursors. Song *et al.* [34] studied the effect of different ZnO seed layers doped with Ga and Al on the growth rate, density, surface area and the diameter of highly oriented ZnO nanorods. Polsongkram and his co-workers [35]

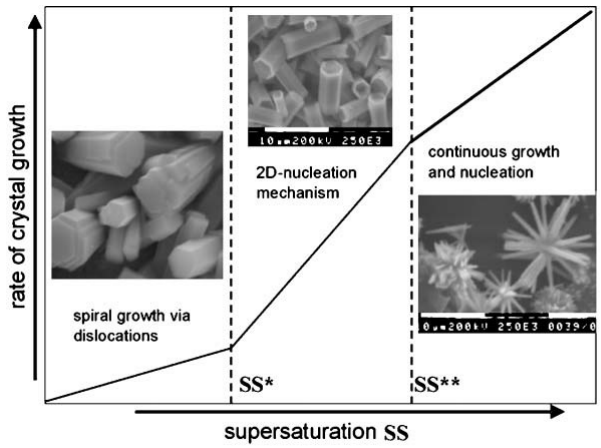

Fig. 2.2 Relationship between supersaturation, morphology and rate of crystal growth in chemical bath deposition. Adapted from Ref [36].

studied the effect of the growth temperature, the concentration of the precursors and the deposition time on the growth of the ZnO nanorods. They found that the morphology and the ordering of the ZnO nanorods were affected by the growth conditions mentioned earlier.

In the CBD method, another factor that needs to be taken into account is the degree of supersaturation, which influences the growth and orientation of the ZnO nanorods. The supersaturation is required for crystallization and to supply the thermodynamic driving force for the spontaneous growth of ZnO nuclei and grains [33]. Crystallization occurs in two steps, namely, nucleation and crystal growth. The supersaturation of a solution depends on the solubility of solids in solution, i.e a higher solubility resulting in lower supersaturation and vice-versa. The effect of the supersaturation on the ZnO nanorod, morphologies is shown in Figure 2.2. As can be seen from Figure 2.2 and at lower supersaturation, the crystal faces grow through the outward displacement and crystals have a polyhedral shape structure [36]. In the intermediate supersaturation range the ZnO grows by a mixture of spiral and 2D nucleation growth with hollowed rod morphology. Finally, at higher supersaturation, the growth of ZnO nanorods occurs linearly, adopting dendritic to spherulitic morphologies [36].

2.3 Nanostructured ZnO

ZnO nanostructured materials have been synthesized as zero dimensional (0D), one dimensional (1D) and two dimensional (2D) structures. 0D ZnO structures, which include quantum dots, core-shell quantum dots, hollow spheres and heterogeneous binary arrays of nanoparticles have already been synthesized by several researchers [37–39]. ZnO structures such as nanorods, nanowires, nanoribbons, nanofibers and nanobelts are categorised as 1D nanostructured materials and have also been studied extensively [40–44]. These 1D nanostructured materials possess a great potential

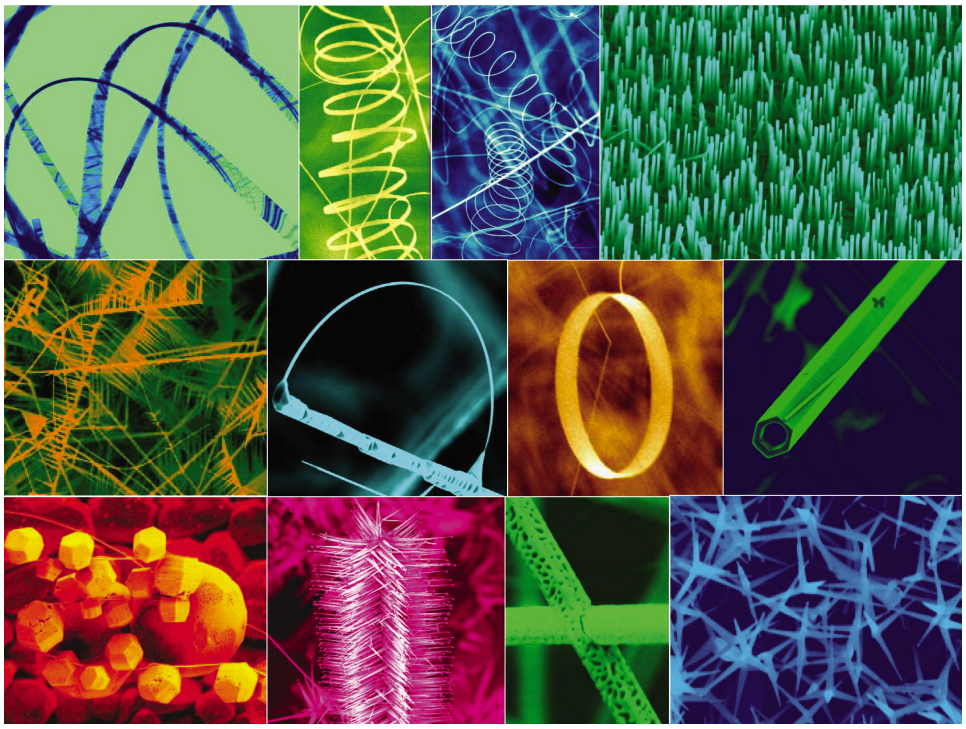

Fig. 2.3 A collection of different ZnO nanostructures synthesized from solid powder under controlled conditions using thermal evaporation technique. Adapted from Ref [47].

interest due to their distinctive physical and chemical properties, and their application in technology. 2D nanostructured materials include nanoplates, nanoprisms, nanosheets, nanodisks and nanowalls [45, 46]. By controlling the growth kinetics, temperature and the composition of the material's precursors, a variety of ZnO nanostructures have been prepared, as shown in Figure 2.3 [47].

2.4 ZnO optical properties

The photoluminescent (PL) properties of ZnO at room temperature excited by UV laser is usually characterized by two emission bands. The first band is located in the UV range (around 380 nm), and it has been attributed to near band edge emission [48]. The second band is the deep-level emission band. It is located in the visible range (450 – 800 nm) and is attributed to the recombination process between electrons and holes due to surface and point defects, such as zinc interstitials, oxygen vacancies and incorporation of hydroxyl groups (because of the solution growth) [49–51]. ZnO also showed a small peak around 760, which is attributed to the second order of the band-edge emission [52, 53]. Recently, rare-earth (Sm and Ce) have been used as dopant to enhance the emission of these two bands (i.e UV and deep-level emission).

2.5 Application of ZnO in Schottky diode devices

Application of ZnO nanostructured materials in metal-semiconductor devices (i.e. Schottky diodes) has attracted much attention due to their simple fabrication [54–56]. ZnO nanostructures have been utilized for the fabrication of light emitting diodes [57], UV photodetectors [58], solar cells [59] and Schottky diode devices [10, 60–62]. Different metals such as Au, Pt, Ag and Ir have been used as rectifying contact to ZnO. Fabrication of high quality ohmic and Schottky contacts is required to improve the performance of ZnO based devices. The formation of such contacts on n-ZnO is rather difficult, because of the presence of oxygen vacancies and zinc interstitials on the surface of ZnO. This problem can be eliminated by treating the surface of ZnO with H_2O_2 or by chemical etching [63, 64]. Moreover, ZnO heterojunction structures have shown remarkable properties that are useful in optoelectronic applications. Such a heterojunction can be achieved by depositing a ZnO layer on p-type materials such as GaN and Si. Furthermore, doped ZnO nanostructured materials have shown to be good Schottky diode devices [65–67]. Mandalapu and his co-workers [68] fabricated hetrojunction diodes and photoconductive devices after doping p-type ZnO with Sb using n-Si(100) substrate. Mehmet Yilmaz [69] fabricated a hetrojunction diode based on Co doped ZnO thin films on a p-type Si substrate. He found that the ideality factor of the fabricated Schottky diode decreased with increasing the Co contents. Yilmaz *et al.* [70] also fabricated a hetrojunction diode devices based on ZnO thin films doped with F using spray pyrolysis and p-Si substrates.

References

[1] Ü. Özgür, Y. I. Alivov, C. Liu, A. Teke, M. Reshchikov, S. Doğan, V. Avrutin, S.-J. Cho, H. Morkoç, A comprehensive review of ZnO materials and devices, J. Appl. Phys. 98 (4) (2005) 11.

[2] J. C. Johnson, H. Yan, P. Yang, R. J. Saykally, Optical cavity effects in ZnO nanowire lasers and waveguides, J. Phys. Chem. B 107 (34) (2003) 8816–8828.

[3] Q. Zhou, C. Sharp, J. Cannata, K. Shung, G. Feng, E. Kim, Self-focused high frequency ultrasonic transducers based on ZnO piezoelectric films, Appl. Phys. Lett. 90 (11) (2007) 113502.

[4] X. Jiang, F. Wong, M. Fung, S. Lee, Aluminum-doped zinc oxide films as transparent conductive electrode for organic light-emitting devices, Appl. Phys. Lett. 83 (9) (2003) 1875–1877.

[5] H. Wang, B. S. Kang, F. Ren, L. Tien, P. Sadik, D. Norton, S. Pearton, J. Lin, Hydrogen-selective sensing at room temperature with ZnO nanorods, Appl. Phys. Lett. 86 (24) (2005) 243503.

References

[6] Y. Zhang, Q. Xiang, J. Xu, P. Xu, Q. Pan, F. Li, Self-assemblies of Pd nanoparticles on the surfaces of single crystal ZnO nanowires for chemical sensors with enhanced performances, J. Mater. Chem. 19 (27) (2009) 4701–4706.

[7] Y. Xu, Y. Li, H. Zhang, L. Jin, X. Fang, L. Shi, L. Xu, X. Ma, Y. Zou, J. Yin, Ultraviolet-enhanced electroluminescence from individual ZnO microwire/p-Si light-emitting diode by reverse tunneling effect, J. Mater. Chem. C 5 (26) (2017) 6640–6646.

[8] O. Harnack, C. Pacholski, H. Weller, A. Yasuda, J. Wessels, Rectifying behavior of electrically aligned ZnO nanorods, Nano Lett. 3 (8) (2003) 1097–1101.

[9] H. von Wenckstern, G. Biehne, R. A. Rahman, H. Hochmuth, M. Lorenz, M. Grundmann, Mean barrier height of Pd Schottky contacts on ZnO thin films, Appl. Phys. Lett 88 (9) (2006) 092102.

[10] L. Rajan, C. Periasamy, V. Sahula, Electrical characterization of Au/ZnO thin film Schottky diode on silicon substrate, Perspect. Sci. 8 (2016) 66–68.

[11] P. Zhu, Z. Weng, X. Li, X. Liu, S. Wu, K. Yeung, X. Wang, Z. Cui, X. Yang, P. K. Chu, Biomedical applications of functionalized ZnO nanomaterials: From biosensors to bioimaging, Adv. Mater. Interfaces 3 (1) (2016) 1500494.

[12] S. Gowrishankar, L. Balakrishnan, N. Gopalakrishnan, Band gap engineering in $Zn_{(1-x)}$ Cd_xO and $Zn_{(1-x)}$ Mg_xO thin films by RF sputtering, Ceram. Int. 40 (1) (2014) 2135–2142.

[13] K. Kim, H. Kim, D. Hwang, J. Lim, S. Park, Realization of p-type ZnO thin films via phosphorus doping and thermal activation of the dopant, Appl. Phys. Lett. 83 (1) (2003) 63–65.

[14] J. Lu, Z. Ye, F. Zhuge, Y. Zeng, B. Zhao, L. Zhu, p-type conduction in N–Al co-doped ZnO thin films, Appl. Phys. Lett. 85 (15) (2004) 3134–3135.

[15] J. Lu, Y. Zhang, Z. Ye, L. Zhu, L. Wang, B. Zhao, Q. Liang, Low-resistivity, stable p-type ZnO thin films realized using a Li–N dual-acceptor doping method, Appl. Phys. Lett. 88 (22) (2006) 222114.

[16] R. Kumar, O. Al-Dossary, G. Kumar, A. Umar, Zinc oxide nanostructures for NO_2 gas–sensor applications: A review, Nano-Micro Lett. 7 (2) (2015) 97–120.

[17] R. Kumar, G. Kumar, A. Umar, Zinc oxide nanomaterials for photocatalytic degradation of methyl orange: A review, Nanosci. Nanotechnol. Lett. 6 (8) (2014) 631–650.

[18] C. Jagadish, S. J. Pearton, Zinc oxide bulk, thin films and nanostructures: processing, properties, and applications, Elsevier, 2011.

[19] W. Lambrecht, A. V. Rodina, S. Limpijumnong, B. Segall, B. Meyer, Valence-band ordering and magneto-optic exciton fine structure in ZnO, Phys. Rev. B 65 (7) (2002) 075207.

[20] S. Li, P. Lin, C. Lee, T. Tseng, Field emission and photofluorescent characteristics of zinc oxide nanowires synthesized by a metal catalyzed vapor-liquid-solid process, J. Appl. Phys. 95 (7) (2004) 3711–3716.

[21] H. Chin, L. Chao, C. C. Wu, Crystal, optical, and electrical characteristics of transparent conducting gallium-doped zinc oxide films deposited on flexible polyethylene naphthalate substrates using radio frequency magnetron sputtering, Mater. Res. Bull. 79 (2016) 90–96.

[22] V. Craciun, J. Elders, J. G. Gardeniers, I. W. Boyd, Characteristics of high quality ZnO thin films deposited by pulsed laser deposition, Appl. Phys. Lett. 65 (23) (1994) 2963–2965.

[23] R. Liu, A. A. Vertegel, E. W. Bohannan, T. A. Sorenson, J. A. Switzer, Epitaxial electrodeposition of zinc oxide nanopillars on single-crystal gold, Chem. Mater. 13 (2) (2001) 508–512.

[24] W. Lee, M. Jeong, J. Myoung, Catalyst-free growth of ZnO nanowires by metal-organic chemical vapour deposition (MOCVD) and thermal evaporation, Acta Mater. 52 (13) (2004) 3949–3957.

[25] J.-J. Wu, S.-C. Liu, Low-temperature growth of well-aligned ZnO nanorods by chemical vapor deposition, Adv. Mater. 14 (3) (2002) 215–218.

[26] S. Studenikin, N. Golego, M. Cocivera, Fabrication of green and orange photoluminescent, undoped ZnO films using spray pyrolysis, J. Appl. Phys. 84 (4) (1998) 2287–2294.

[27] Y. Natsume, H. Sakata, Zinc oxide films prepared by sol-gel spin-coating, Thin Solid Films 372 (1-2) (2000) 30–36.

[28] P. Hari, M. Baumer, W. Tennyson, L. Bumm, ZnO nanorod growth by chemical bath method, J. Non-cryst. Solids 354 (19-25) (2008) 2843–2848.

[29] B. G. Rao, D. Mukherjee, B. M. Reddy, Novel approaches for preparation of nanoparticles, in: Nanostructures for Novel Therapy, Elsevier, 2017, pp. 1–36.

[30] R. J. Corriu, D. Leclercq, Recent developments of molecular chemistry for sol–gel processes, Angewandte Chem. Int. Edn 35 (13-14) (1996) 1420–1436.

[31] L. Hench, J. West, The sol-gel process, Chem. Rev. 90 (1) (1990) 33–72.

[32] L. E. Greene, M. Law, J. Goldberger, F. Kim, J. C. Johnson, Y. Zhang, R. J. Saykally, P. Yang, Low-temperature wafer-scale production of ZnO nanowire arrays, Angewandte Chem. Int Edn 42 (26) (2003) 3031–3034.

[33] Y. Liu, W. Gao, Growth process, crystal size and alignment of ZnO nanorods synthesized under neutral and acid conditions, J. Alloy Compd. 629 (2015) 84–91.

[34] J. Song, S. Lim, Effect of seed layer on the growth of ZnO nanorods, J. Phys. Chem. C 111 (2) (2007) 596–600.

References

[35] D. Polsongkram, P. Chamninok, S. Pukird, L. Chow, O. Lupan, G. Chai, H. Khallaf, S. Park, A. Schulte, Effect of synthesis conditions on the growth of ZnO nanorods via hydrothermal method, Physica B: Condens. Matter 403 (19-20) (2008) 3713–3717.

[36] K. Govender, D. S. Boyle, P. B. Kenway, P. O'Brien, Understanding the factors that govern the deposition and morphology of thin films of ZnO from aqueous solution, J. Mater. Chem. 14 (16) (2004) 2575–2591.

[37] K. Lin, H. Cheng, H. Hsu, L. Lin, W. Hsieh, Band gap variation of size-controlled ZnO quantum dots synthesized by sol–gel method, Chem. Phys. Lett. 409 (4-6) (2005) 208–211.

[38] H. Zhou, T. Fan, D. Zhang, Hydrothermal synthesis of ZnO hollow spheres using spherobacterium as biotemplates, Micropor. Mesopor. Mater. 100 (1-3) (2007) 322–327.

[39] G. Zhang, D. Wang, Fabrication of heterogeneous binary arrays of nanoparticles via colloidal lithography, J. Am. Chem. Soc. 130 (17) (2008) 5616–5617.

[40] J. Lu, Z. Shi, Y. Wang, Y. Lin, Q. Zhu, Z. Tian, J. Dai, S. Wang, C. Xu, Plasmon-enhanced electrically light-emitting from ZnO nanorod arrays/p-GaN heterostructure devices, Sci Rep. 6 (2016) 25645.

[41] A. Di Mauro, M. Zimbone, M. E. Fragalà, G. Impellizzeri, Synthesis of ZnO nanofibers by the electrospinning process, Mater. Sci. Semicond. Process. 42 (2016) 98–101.

[42] Z. W. Pan, Z. R. Dai, Z. L. Wang, Nanobelts of semiconducting oxides, Sci. 291 (5510) (2001) 1947–1949.

[43] H. Yan, J. Johnson, M. Law, R. He, K. Knutsen, J. R. McKinney, J. Pham, R. Saykally, P. Yang, ZnO nanoribbon microcavity lasers, Adv. Mater. 15 (22) (2003) 1907–1911.

[44] L. Vayssieres, Growth of arrayed nanorods and nanowires of ZnO from aqueous solutions, Adv. Mater. 15 (5) (2003) 464–466.

[45] S. Vizireanu, S. Stoica, C. Luculescu, L. Nistor, B. Mitu, G. Dinescu, Plasma techniques for nanostructured carbon materials synthesis. A case study: carbon nanowall growth by low pressure expanding RF plasma, Plasma Sourc. Sci. Tech. 19 (3) (2010) 034016.

[46] J. N. Tiwari, R. N. Tiwari, K. S. Kim, Zero-dimensional, one-dimensional, two-dimensional and three-dimensional nanostructured materials for advanced electrochemical energy devices, Progress Mater. Sci. 57 (4) (2012) 724–803.

[47] Z. L. Wang, Nanostructures of zinc oxide, Mater. Today 7 (6) (2004) 26–33.

[48] S. C. Lyu, Y. Zhang, H. Ruh, H. Lee, H. Shim, E. Suh, C. J. Lee, Low temperature growth and photoluminescence of well-aligned zinc oxide nanowires, Chem. Phys. Lett. 363 (1-2) (2002) 134–138.

[49] L. Xu, Y. Guo, Q. Liao, J. Zhang, D. Xu, Morphological control of ZnO nanostructures by electrodeposition, J. Phys. Chem. B 109 (28) (2005) 13519–13522.

[50] K. Tam, C. Cheung, Y. Leung, A. Djurišić, C. Ling, C. Beling, S. Fung, W. Kwok, W. Chan, D. Phillips, et al., Defects in ZnO nanorods prepared by a hydrothermal method, J. Phys. Chem. B 110 (42) (2006) 20865–20871.

[51] Y. J. Kim, H. Shang, G. Cao, Growth and characterization of [001] ZnO nanorod array on ITO substrate with electric field assisted nucleation, J. Sol-Gel Sci. Techn. 38 (1) (2006) 79–84.

[52] C. Tonon, C. Duvignacq, G. Teyssedre, M. Dinguirard, Degradation of the optical properties of ZnO-based thermal control coatings in simulated space environment, J. Phys. D Appl. Phys. 34 (1) (2001) 124.

[53] T. Mahalingam, K. M. Lee, K. H. Park, S. Lee, Y. Ahn, J.-Y. Park, K. H. Koh, Low temperature wet chemical synthesis of good optical quality vertically aligned crystalline ZnO nanorods, Nanotech. 18 (3) (2007) 035606.

[54] C. S. Lao, J. Liu, P. Gao, L. Zhang, D. Davidovic, R. Tummala, Z. L. Wang, ZnO nanobelt/nanowire Schottky diodes formed by dielectrophoresis alignment across Au electrodes, Nano Lett. 6 (2) (2006) 263–266.

[55] J. Yu, S. Ippolito, W. Wlodarski, M. Strano, K. Kalantar-Zadeh, Nanorod based Schottky contact gas sensors in reversed bias condition, Nanotech. 21 (26) (2010) 265502.

[56] A. Dey, A. Layek, A. Roychowdhury, M. Das, J. Datta, S. Middya, D. Das, P. P. Ray, Investigation of charge transport properties in less defective nanostructured ZnO based Schottky diode, RSC Adv. 5 (46) (2015) 36560–36567.

[57] A. Tsukazaki, A. Ohtomo, T. Onuma, M. Ohtani, T. Makino, M. Sumiya, K. Ohtani, S. F. Chichibu, S. Fuke, Y. Segawa, et al., Repeated temperature modulation epitaxy for p-type doping and light-emitting diode based on ZnO, Nat. Mater. 4 (1) (2005) 42.

[58] Y. Lin, C. Chen, W. Yen, W. Su, C. Ku, J. Wu, Near-ultraviolet photodetector based on hybrid polymer/zinc oxide nanorods by low-temperature solution processes, Appl. Phys. Lett. 92 (23) (2008) 205.

[59] S. Major, K. Chopra, Indium-doped zinc oxide films as transparent electrodes for solar cells, Solar Energy Mater. 17 (5) (1988) 319–327.

[60] H. Sheng, S. Muthukumar, N. Emanetoglu, Y. Lu, Schottky diode with Ag on (1120) epitaxial ZnO film, Appl. Phys. Lett. 80 (12) (2002) 2132–2134.

[61] S. Kim, B. Kang, F. Ren, K. Ip, Y. Heo, D. Norton, S. Pearton, Sensitivity of Pt/ZnO Schottky diode characteristics to hydrogen, Appl. Phys. Lett. 84 (10) (2004) 1698–1700.

References

[62] L. Brillson, Y. Lu, ZnO Schottky barriers and Ohmic contacts, J. Appl. Phys. 109 (12) (2011) 8.

[63] Z. Song, H. Zhou, C. Ye, L. Yang, M. Xue, J. Mei, H. Wang, Surface treatment for Schottky barrier photodetector based on Au/GaZnO nanorods/Au structure, Mater. Sci. Semicond. Process. 64 (2017) 101–108.

[64] R. Yatskiv, J. Grym, Influence of the interaction between graphite and polar surfaces of ZnO on the formation of Schottky contact, J. Electron. Mater. 47 (9) (2018) 5002–5006.

[65] M. Yilmaz, Z. Caldiran, A. Deniz, S. Aydogan, R. Gunturkun, A. Turut, Preparation and characterization of sol–gel-derived n-ZnO thin film for Schottky diode application, Appl. Phys. A 119 (2) (2015) 547–552.

[66] M. Yilmaz, Ş. Aydoğan, The effect of Mn incorporation on the structural, morphological, optical, and electrical features of nanocrystalline ZnO thin films prepared by chemical spray pyrolysis technique, Metall. Mater. Trans. A 46 (6) (2015) 2726–2735.

[67] Ş. Aydoğan, M. L. Grilli, M. Yilmaz, Z. Çaldiran, H. Kaçuş, A facile growth of spray based ZnO films and device performance investigation for Schottky diodes: determination of interface state density distribution, J. Alloy Compd. 708 (2017) 55–66.

[68] L. Mandalapu, F. Xiu, Z. Yang, J. Liu, Al/Ti contacts to Sb-doped p-type ZnO, J. Appl. Phys. 102 (2) (2007) 023716.

[69] M. Yilmaz, A function of external doping: Characteristics of inorganic nanostructure based diode, Ceram. Int. 45 (1) (2019) 665–673.

[70] A. Özmen, S. Aydogan, M. Yilmaz, Fabrication of spray derived nanostructured n-ZnO/p-Si heterojunction diode and investigation of its response to dark and light, Ceram. Int. 45 (12) (2019) 14794–14805.

Chapter 3

Theoretical background

3.1 Metal semiconductor contacts

3.1.1 Introduction

The quality of the metal-semiconductor contact plays an important and critical role in device performance and integrated circuits. They are very important in understanding the fundamental physical properties such as defects and interface properties of a semiconductor device. Metal-semiconductor contacts were investigated as early as 1874 by Braun. He found that the total resistance depends on the polarity of the applied bias voltage and the detailed surface conditions. Later Schottky and Mott proposed a model known as diffusion theory for the current transport for the fabricated Schottky diode device [1]. Before 1960 the use of the Schottky diode was limited to frequency conversion and microwave devices. After 1960 to date, metal-semiconductor contacts have been studied extensively. They have been used in devices such as solar cells, photodetectors and as electrodes for MESFETs. Metal-semiconductor contacts are divided into two types according to their use in device fabrication and integrated circuits namely: *ohmic* and *rectifying* contacts.

3.1.2 Band bending

When a metal is brought into contact with an n-type semiconductor, electrons will lower their energy by moving from the semiconductor (i.e. conduction band) to the metal. Due to the difference in their work functions[1] and as a result, a build up of charge close to the metal-semiconductor interface will cause deformation of the band edges until thermal equilibrium is reached where the Fermi levels of the two substances coincide with each other (see Figure 3.1) [2]. The bending or the deformation of the band will form a potential barrier which electrons need to overcome in order to flow from

[1] The work function of a material is the minimum energy required for an electron from the Fermi level the vacuum level.

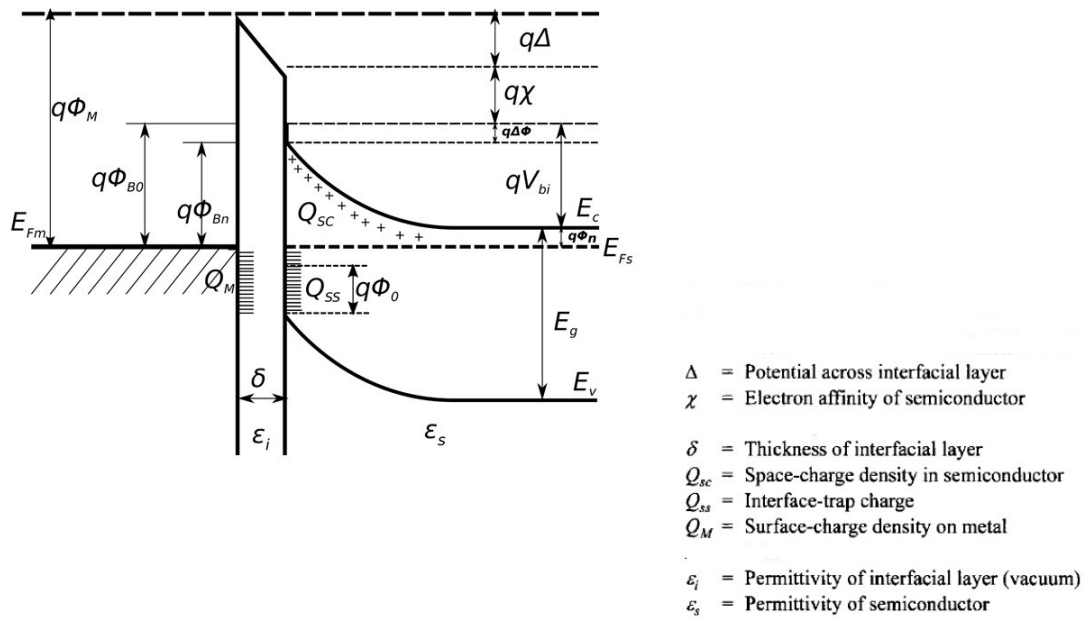

Fig. 3.1 Energy band diagram of a metal- n-type semiconductor contact with an interfacial layer and interface trap charge. Redrawn from Ref [3].

semiconductor to the metal. A schematic of the energy band diagram of metal and semiconductor with an interfacial layer is shown in Figure 3.1. As electrons flow from the semiconductor into the metal, a region depleted of electrons will be formed, which is known as the depletion region.

3.1.3 Ohmic contacts

The ohmic contact is defined as metal-semiconductor contacts that have linear *I-V* characteristics regardless of the polarity of the applied bias voltage [4]. The ohmic contact must have low resistance and not significantly affect the device performance due to the voltage drop across the contact [5]. According to the Schottky model, when a metal is brought into contact with a semiconductor, the contact character (rectifying or ohmic) depends on the electron affinity of the semiconductor and the work function of the metal. The ideal ohmic contact is a contact that allows the charge carriers to freely move in either direction across the contact with a zero or minimal resistance. In order to fabricate an ohmic contact on a semiconductor (n-type semiconductor, see Figure 3.2 (a)), the work function of the metal must be smaller or close to the electron affinity of the semiconductor, and the barrier height will be zero or negligible as shown in Figure 3.2 (b).

For a p-type semiconductor, the metal work function must be larger or close to the sum of the band gap energy and electron affinity in order for an ohmic contact to be formed [5]. After the alignment between the Fermi levels of the metal and semiconductor, the carriers can flow easily between metal and semiconductor with small resistance across the contact. Ohmic contacts can be classified into

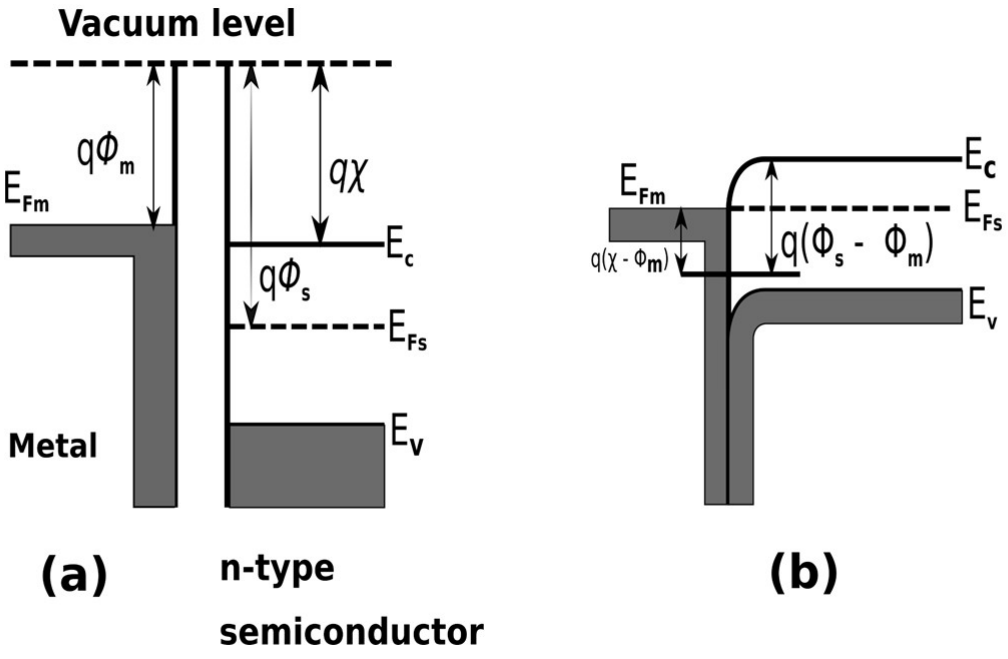

Fig. 3.2 An ohmic contact on the n-type semiconductor with $\Phi_M < \Phi_S$ (a) before contact and (b) after intimate metal contact with the semiconductor. Redrawn from Ref [6].

three types: *tunnel*, *alloyed* and *annealed* contacts. Tunnel contacts are the most practical ones with a positive barrier formed at the metal-semiconductor interface. These contacts have a high enough doping (10^{19} cm^{-3} or higher) in the semiconductor that there is only a thin barrier ($\approx$ 3 nm or less) separating the metal and semiconductor, and carriers can easily tunnel through such a barrier [7]. Alloyed and annealed contacts are obtained by high-temperature treatment of the contacts so as to minimize the unintentional barrier at the interface, or that the deposited metals can alloy with the semiconductor. The annealing is performed in a controlled atmosphere (e.g. N, Ar or a combination of H and N) to reduce the interfacial oxide layer between the semiconductor and the metal and also to avoid metal oxidation during the annealing process. As mentioned earlier in this section, choosing a specific metal to form an ohmic contact depends on the work function of that specific metal. However, choosing the right work function of the metal does not always ensure a perfect ohmic contact because of Fermi level pinning at the interface caused by the large number of surface states at the interface [7]. This pinning means that, in practice, a tunnel contact is the practical ohmic contact with low resistance.

3.1.4 Schottky contacts

A Schottky contact is a rectifying metal-semiconductor contact. It allows current to flow freely under forward bias and allows a negligible current to flow under reverse bias. When a metal and semiconductor are joined together, the Fermi energies of the metal and the semiconductor coincide at thermal equilibrium, forming a barrier, as shown in Figure 3.1.

For a Schottky barrier to be formed there must be a difference in potential between the Fermi energy level of the metal and the semiconductor band edge where carriers are found (neglecting the effect of interface and surface states). This barrier height Φ_B for an n-type and p-type semiconductor is given by Equation 3.1 and Equation 3.2, respectively [8]:

$$\Phi_{Bn} = \Phi_m - \chi_s \tag{3.1}$$

$$\Phi_{Bp} = \frac{E_g}{q} + \chi_s - \Phi_m \tag{3.2}$$

where, Φ_{Bn}, Φ_{Bp} and χ_s are the barrier height of n-type, p-type and electron affinity of the semiconductor, respectively, and Φ_m is the work function of the metal, and the energy gap of the semiconductor is denoted by E_g. Generally, the barrier height is affected by the presence of surface and interface states, and also the presence of an interfacial layer at the metal-semiconductor interface.

3.1.5 Forward and reverse bias

Under applied forward bias ($V > 0$) the Fermi energy of the semiconductor is raised with respect to that of the metal as shown in Figure 3.3 (a). Consequently, for electrons moving from the semiconductor to the metal there will be a smaller barrier (V_0-V) compared to the unbiased junction (V_0), while the barrier seen by electrons moving from the metal to the semiconductor does not change. Consequently, electrons will cross the barrier more easily from the semiconductor to the metal compared to those that drift from the metal to the semiconductor. This leads to a large current flowing through the device due to the majority charge carriers. Note that the barrier height of the metal in case of forward bias is unaffected by the applied voltage bias, because there is practically no voltage drop across the metal as all the excess charge accumulates at the surface [9].

Under reverse bias ($V < 0$) the Fermi energy of semiconductor is lowered with respect to the metal, as illustrated in Figure. 3.3 (b) and as the result both energy levels of the conduction and valence bands are lowered. This means that the potential barrier as seen by electrons travelling from the semiconductor towards the metal increases and as the result, charge carriers will have difficulty in crossing the barrier. This results in an increase in depletion width. Thus, current flowing from the semiconductor to the metal is reduced while the opposite current (i.e. from metal to semiconductor) remains practically unchanged. This means that a smaller current is flowing from semiconductor to

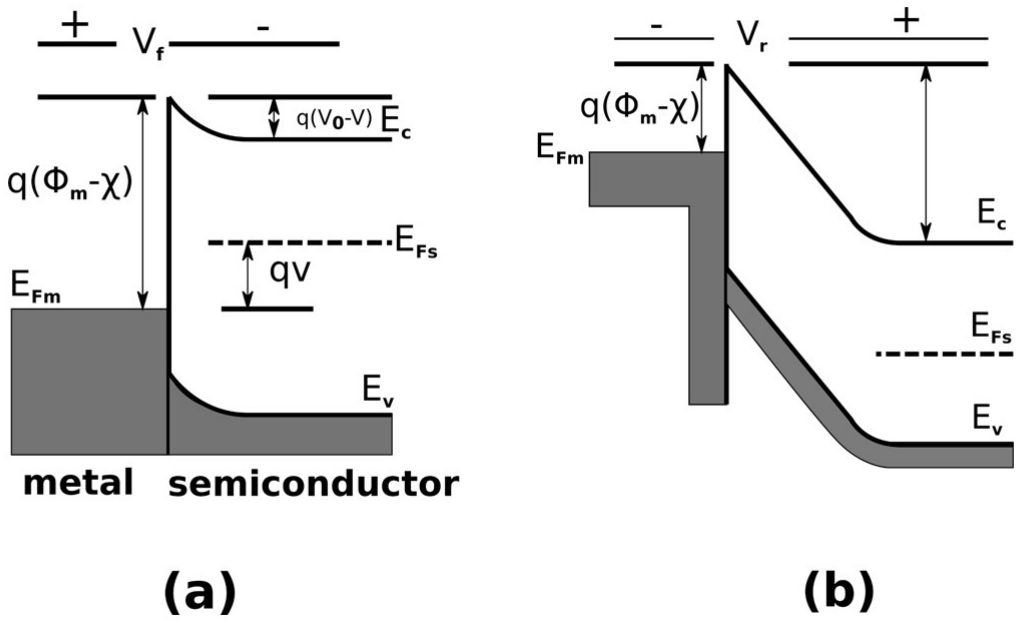

Fig. 3.3 Metal-semiconductor energy band diagram under (a) forward bias and (b) reverse bias. Redrawn from Ref [3].

metal at the interface compared to the forward current [9]. As previously, the barrier seen by electrons moving from the metal to the semiconductor is unchanged. Therefore, the contact is said to be a rectifying contact.

3.1.6 Barrier height determination

The barrier height of metal-semiconductor contacts can be determined using four methods, namely, current-voltage, capacitance-voltage, activation energy and photoelectric methods. The first two methods are the most commonly used, and were employed in this study, as will be outlined in the following subsections.

3.2 Current - voltage characteristics of a Schottky barrier

The current-voltage (*I-V*) measurement is used in the investigation of the quality of the contacts, as well as determining the Schottky barrier height Φ_B at room temperature, by assuming that current transport mechanism across the potential barrier is thermionic emission. For different temperatures other transport mechanisms such as tunneling and generation recombination may also contribute to the flow of the charge carriers within the depletion region [10]. The current flowing according to

thermionic emission is given by the following expression:

$$I = I_s[\exp\left(\frac{qV}{nkT}\right) - 1] \tag{3.3}$$

where

$$I_s = AA^*T^2\exp\left(-\frac{q\Phi_B}{kT}\right). \tag{3.4}$$

Equations 3.3 and 3.4 are for the ideal Schottky diode where the series resistance is neglected. The Schottky barrier height calculated from I_s (saturation current) by extrapolating the ln$I$ vs V curve to V = 0 is given by [10]

$$\Phi_B = \frac{kT}{q}\ln\left(\frac{AA^*T^2}{I_s}\right) \tag{3.5}$$

where A and A^* are the diode contact area and the effective Richardson constant, respectively. However, in the case of non-ideal diodes, the current transport in the diode is no longer dominated by a thermionic emission current only and other mechanisms may be involved. In this case the series resistance is too large to neglect and the ideality factor will depart from unity. Therefore Equations 3.3 and 3.4 are often not applicable to actual Schottky diodes. In the following subsections a detailed overview of the effect of temperature on different current transport mechanisms and the calculation of barrier height are outlined.

3.3 Current transport mechanisms

The current transport in Schottky diode devices is mainly due to majority carriers, unlike in the p-n junction where the minority carriers play a larger role [3]. There are three main transport mechanisms in the Schottky barrier by which the charge carriers can flow under an applied forward bias [3, 11]. These mechanisms include thermionic emission, generation recombination in the depletion region and quantum tunnelling. These current transport mechanisms are discussed in detail in the following subsections. In a given Schottky diode device, all three mechanisms can be involved but often one current transport mechanism dominates under specific conditions.

3.3.1 Thermionic emission

Thermionic emission is the dominant process in Schottky diode device at a moderate temperatures (i.e. 300 K) in a moderately doped semiconductor (carrier concentration $\leq 10^{17}$ cm^{-3}). This mechanism is based on the theory derived by Bethe on following four assumptions: (1) Φ_{Bn} is much greater than

kT, (2) thermal equilibrium is established at the planes that determine the emission, (3) the existence of a net current flow does not affect the thermal equilibrium, and (4) the two current fluxes from metal to semiconductor and vice versa can be superimposed [3]. According to this theory, only electrons with energy larger than the top of the barrier will cross the barrier, provided that they move towards the barrier [7]. Due to the above-mentioned assumptions, the shape of the barrier profile is immaterial, and the flow of the current depends only on the barrier height [3]. Now the current density between semiconductor and metal can be given by the following expression:

$$J_{s\to m} = \int_{E_{F_n}+q\Phi_B}^{\infty} q v_x dn \tag{3.6}$$

where $E_{F_n} + q\Phi_B$ and v_x are the required minimum energy for thermionic emission into the metal and the carrier velocity in the transport direction, respectively. The density of electrons in an incremental energy range is expressed as [3]:

$$dn = N(E)F(E)dE \tag{3.7}$$

$$dn \approx \frac{4\pi(2m^*)^{3/2}}{h^3}\sqrt{E-E_C}\exp\left(-\frac{E-E_C+qV_n}{kT}\right)dE \tag{3.8}$$

where $N(E)$, $F(E)dE$, m^* represent the density of the states, distribution function and the effective mass of the electron, respectively, qV_n represents $(E_C - E_F)$, and the Plank constant is denoted by h. If we assume that all energy of the electrons in the conduction band is kinetic energy, then

$$E - E_C = \frac{1}{2}m^*v^2 \tag{3.9}$$

$$dE = m^*vdv \tag{3.10}$$

$$\sqrt{E-E_C} = v\sqrt{m^*/2} \tag{3.11}$$

Now Equation 3.8 can be written as [3]

$$dn = 2\left[\frac{m^*}{h}\right]^3 \exp\left(-\frac{qV_n}{kT}\right)\exp\left(-\frac{m^*v^2}{2kT}\right)[4\pi v^2 dv] \tag{3.12}$$

Equation 3.12 describes the number of electrons per unit volume having speeds in the range v and $v+dv$ distributed all over directions [8]. By resolving into velocity components (v_x, v_y and v_z) with the x-axis being parallel to the transport direction, then

$$v^2 = v_x^2 + v_y^2 + v_z^2, \tag{3.13}$$

and by using the transformation $4\pi v^2 dv = dv_x dv_y dv_z$, the current density in Equation 3.6 using Equation 3.12 can be written as:

$$J_{s\to m} = \left[\frac{4\pi q m^* k^2}{h^3}\right] T^2 \exp\left[-\frac{qV_n}{kT}\right] \exp\left[-\frac{m^* v_{ox}^2}{2kT}\right] \tag{3.14}$$

The minimum velocity v_{ox} in the x-direction to surmount the barrier height is

$$v_{ox} = \frac{2q(V_{bi} - V)}{m^*} T^2 \tag{3.15}$$

where V_{bi} is the built in voltage at zero applied bias. By substituting Equation 3.15 into Equation 3.14 we obtain [8]

$$J_{s\to m} = \left[\frac{4\pi q m^* k^2}{h^3}\right] \exp\left[-\frac{q(V_n + V_{bi})}{2kT}\right] \exp\left[\frac{qV}{kT}\right] \tag{3.16}$$

$$= A^* \exp\left(-\frac{q\Phi_B}{kT}\right) \exp\left(\frac{qV}{kT}\right) \tag{3.17}$$

The effective Richardson constant for thermionic emission is given by $\frac{4\pi q m^* k^2}{h^3}$ and Φ_B is the barrier height, which is the sum of V_n and V_{bi}. For the free electrons ($m^* = m_0$), A^* = 120 A/cm^2 K^2. Under applied bias, the barrier height remains the same for electrons that move from the metal into the semiconductor, and thus the current flowing to the semiconductor from metal is unaffected by the applied bias. This current, therefore, must be equal to the current flowing into the metal from the semiconductor at equilibrium ($V = 0$). The equivalent current density is given by [8]

$$J_{m\to s} = -A^* T^2 \exp\left(-\frac{q\Phi_B}{kT}\right) \tag{3.18}$$

Now the total current density for an n-type semiconductor J_n is the sum of the current density flowing from semiconductor to metal and vice versa. Thus [8]

$$J_n = \left(A^* T^2 \exp\left[-\frac{q\Phi_{Bn}}{kT}\right] \exp\left[\frac{qV}{kT}\right] - 1\right) \tag{3.19}$$

$$= J_{TE}\left(\exp\left(\frac{qV}{kT}\right) - 1\right) \tag{3.20}$$

where J_{TE} is the saturation current density for an ideal diode neglecting the effect of series resistance R_s which is given by [8]

$$J_{TE} = A^* T^2 \exp\left[-\frac{q\Phi_{Bn}}{kT}\right] \tag{3.21}$$

By considering the effect of R_s (non-ideal diode) and another factor, the ideality factor of the diode n (which is calculated as the gradient of the slope from the linear portion in the I-V characteristics), then Equation 3.20 becomes [8]

$$J_n = J_{TE} \exp\left(\frac{q(V - IR_s)}{nkT}\right)\left(1 - \exp[-\frac{q(V - IR_s)}{kT}]\right) \tag{3.22}$$

and R_s and n are given by

$$n = \frac{q}{kT}\left(\frac{dV}{d(\ln I)}\right) \tag{3.23}$$

$$R_s = \frac{\Delta V}{I} \tag{3.24}$$

3.3.2 Generation recombination

This current is due to electron-hole pair generation and recombination within the space charge region and occurs mainly at low temperature and low applied voltage [9]. Usually, the recombination takes place via localized states, and the most effective centres are those with energies that fall within the middle of the band gap [12]. There are two types of processes in which the recombination can occur, direct and indirect recombination. In direct recombination, an electron from the conduction band and a hole from the valence band can recombine directly (band to band recombination). Direct recombination usually happens in a direct band gap semiconductor as a radiative transition. Note that the location of these electrons and holes that undergo the recombination process are close to the band edges of the semiconductor. In indirect recombination an electron falls into a deep trap which it occupies. These electrons that occupy the traps can fall in a second step to the valence band where they recombine with holes. The theory of the current due to this type of recombination in Schottky diodes is the same as for the p-n junction [12]. The current density at low applied forward bias is given by [12]

$$J_r = J_{r_0} \exp\left[\frac{qV}{2kT}[1 - \exp(\frac{-qV}{kT})]\right] \tag{3.25}$$

where

$$J_{r_0} = \frac{qn_iW}{2\tau_r}. \tag{3.26}$$

Here n_i represents the concentration of the intrinsic electrons, proportional to $(\exp(\frac{-qE_g}{2kT}))$, and τ_r is the life-time of the electron within the depletion width. The current density for the recombination process in Equation 3.26 is obtained following the assumption that the energy levels of the trap centres and the intrinsic level, E_i coincide, that the capture cross sections for holes and electrons are equal, and that the centres are distributed in a uniform manner [12].

3.3.3 Quantum mechanical tunneling

Tunnelling is the process by which the carriers can pass through the junction barrier. For heavily doped semiconductors and at low operational temperature, tunnelling is the dominant transport mechanism [8]. Tunnelling through the barrier junction can occur in two ways, namely, field emission (FE) and thermionic field emission (TFE). In the FE process, the semiconductor is assumed to be degenerate so that the Fermi level is located above the conduction band. Since the semiconductor is heavily doped, the depletion region becomes very thin, and at low temperatures, only electrons with energies near to the Fermi level can tunnel to the metal from the semiconductor [9]. The TFE process dominates at higher temperatures in which electrons will be excited to energy levels above the Fermi energy where they will see a lower and thinner barrier through which they tunnel into the metal. Because the concentration of these excited electrons with an energy above the Fermi level decreases rapidly with increasing energy, there is maximum energy E_m at which the contributions from excited carriers to the TFE reaches the maximum. If the temperature is raised gradually, the energy maximum is reached, and practically all electrons can now overcome the barrier by thermionic emission (Schottky diode mechanism) [9]. The following relationship describes the tunnelling current density:

$$J_t = \exp\left[-\frac{q\Phi_{Bn}}{E_{00}}\right] \tag{3.27}$$

where

$$E_{00} = \frac{q\hbar}{2}\sqrt{\frac{N_d}{\varepsilon_s m^*}} \tag{3.28}$$

where N_d is the electron concentration, ε_s is the permittivity of the semiconductor and E_{00} represents the characteristic energy levels [10].

3.3.4 Image force lowering

The image force lowering, also known as the Schottky barrier-lowering, is the lowering of the barrier energy due to the image force experienced by carriers in the semiconductor. Suppose that we have a metal-vacuum system. The minimum energy required for an electron to be excited from the Fermi energy level into the vacuum is defined as the work function $q\Phi_m$. Consider an electron located at a distance x from the metal-semiconductor interface in the semiconductor; a positive charge will be induced on the surface of the metal [3]. An attractive force will occur between the electron and an induced positive charge at the metal surface. This attraction force is equivalent to the force existing between an electron at a distance x and a positive charge at a distance $-x$ from the interface. The image force lowering effect is shown in Figure 3.4.

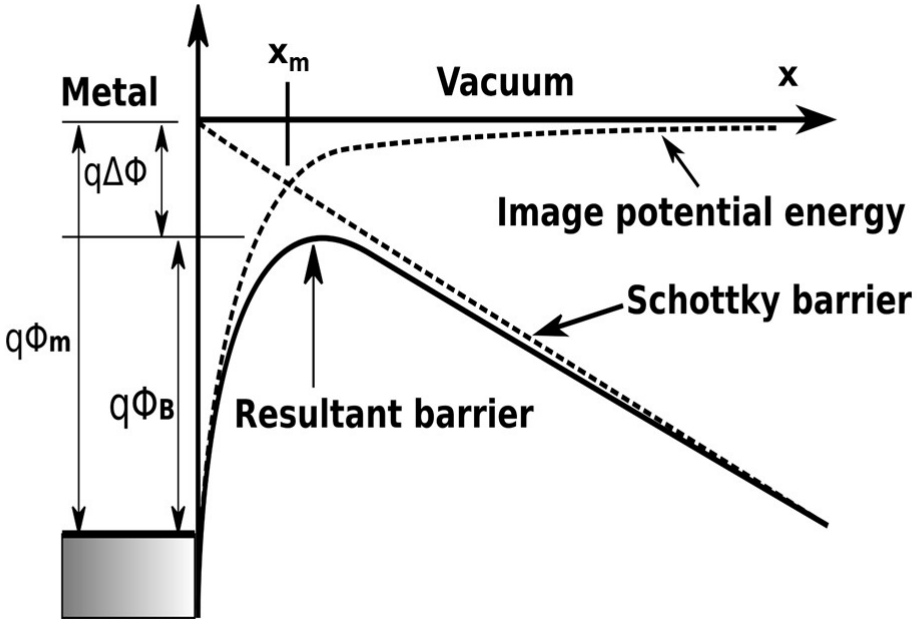

Fig. 3.4 Energy band diagram between a vacuum and metal surface. The Schottky barrier is lowered due to the image force.

The positive charge is defined as the image charge and the attractive force which is referred to as the image force, and is given by:

$$F = \frac{-q^2}{4\pi\varepsilon_0(2x)^2} = \frac{-q^2}{16\pi\varepsilon_0(x)^2} \tag{3.29}$$

where ε_0 and q represent the free space permittivity and electron charge, respectively. The potential energy of the electron is minus the work done on the electron when moving it from infinity to point x and given by

$$PE(x) = \int_{\infty}^{x} F dx = \frac{q^2}{16\pi\varepsilon_0(x)}. \tag{3.30}$$

The calculated energy in the equation above corresponds to the electron's potential energy at a distance x. The total potential energy under an applied external electric field (E_{app}) as a function of a distance measured from the metal surface is given by:

$$PE(x) = \frac{q^2}{16\pi\varepsilon_0 x} + qE_{app}x \tag{3.31}$$

The image force lowering (Schottky barrier lowering) $\Delta\Phi$ may be calculated by first determining the position of the maximum in the barrier x_m where $(d(PE(x))/dx) = 0$ or

$$\Delta\Phi = \sqrt{\frac{q}{16\pi\varepsilon_0 E_{app}}} = 2E_{app}x_m \tag{3.32}$$

$$x_m = \sqrt{\frac{qE_{app}}{4\pi\varepsilon_0}} \tag{3.33}$$

At a position x the maximum potential energy occurs where the resultant electric field equals zero; i.e. the electric field due to the image force is equal to the field in the depletion region but in the opposite direction. By assuming the absence of an interfacial layer between semiconductor and metal, and by applying the Schottky effect to the metal-semiconductor contact, the induced or image charge will be positioned in the semiconductor at a distance x_m from the metal. Note that the electric field in the metal-semiconductor contact is not zero even in the absence of an applied bias because of the built-in potential [3]. By replacing the electric field (E_{app}) by the maximum field at the interface (ζ) and ε_0 by the permittivity of the semiconductor ε_s, the lowering in the Schottky barrier will be given by:

$$\Delta\Phi = \sqrt{\frac{q}{16\pi\varepsilon_s\zeta}} \tag{3.34}$$

The value of ε_s may be different from the static permittivity of the semiconductor. If the transit time of electron from the metal-semiconductor interface to the barrier maximum x_m is shorter than the relaxation time of the dielectric, then the semiconductor medium does not have time to be polarized, and a smaller permittivity value is expected than the static values [3]. The Schottky barrier lowering is

dependent on the applied electric field. Under forward bias, the image force and the field are smaller, and the barrier height is slightly larger than the one at zero bias. In the case of reverse bias, the barrier height is smaller and depends on the applied bias voltage.

3.4 Capacitance voltage measurements

Beside the *I-V* characteristics, capacitance-voltage (*C-V*) characteristics are a common and convenient method for evaluating the quality of Schottky diodes and determining the barrier height, built-in voltage as well as the net doping density of a metal-semiconductor contact [3]. The *C-V* method assumes that the depletion region width of a semiconductor junction depends on the applied bias voltage [3]. When a small voltage (few mV) is superimposed upon an applied dc bias, charges are induced on both the metal side and semiconductor side in such a way that the total charge is zero. In this case, the depletion region may be considered to act as a parallel plate capacitor within the depletion region which acts as dielectric. Upon applying a reverse bias, a small signal capacitance is generated which varies with the applied bias voltage. The *C-V* characteristics can also be used to study impurity levels and their distribution within the semiconductor, which helps in designing quality semiconductor devices and improve their operation. The square root of the capacitance per unit area of an n-type metal-semiconductor contact Schottky barrier diode is given by [9]

$$\frac{1}{C^2} = \left(\frac{2}{\varepsilon_s \varepsilon_0 q N_{dcv} A^2}\right)\left(V_{bi} - V - \frac{kT}{q}\right) \tag{3.35}$$

where q, N_d, V, V_{bi} are the electronic charge, free carrier concentration, applied voltage and the built-in voltage, respectively. According to this method N_d is assumed to be much greater than N_A. Care needs to be taken when measuring the diode contact area as it affects by a factor squared [10]. In the derivation of Equation 3.35 it is assumed that the donor concentration has a uniform distribution and the interfacial oxide layer is negligible. The free carrier concentration (net doping density) is obtained from the plot of $1/C^2$ against the applied bias voltage using the following procedure. The barrier height is related to the built-in voltage by

$$\Phi_B = V_{bi} + V_0 \tag{3.36}$$

where

$$V_0 = \frac{kT}{q}\ln(\frac{N_c}{N_d}) \tag{3.37}$$

Here N_c is the effective density of states in the conduction band. By plotting $\frac{1}{C^2}$ versus applied voltage V a curve is obtained with the slope $\frac{2}{-q\varepsilon_0\varepsilon_s N_d}$ and intercept on the voltage-axis, $V_0 = V_i - kT/q$,

and the built-in voltage (V_{bi}) is given by $V_{bi} = -V_i + \frac{kT}{q}$. Then, the slope of the straight line can be used to determine the N_d and the barrier height, Φ_B is obtained from V_i using

$$\Phi_B = V_0 - V_i + \frac{kT}{q} \tag{3.38}$$

The addition of the factor kT/q in the above equation is due to the contribution of the majority carriers to the space charge [9]. Note that the above equation does not take into consideration the effect of the barrier height lowering and image force lowering.

3.5 Surface states

Surface states are localized states known as the electronic states that are usually found at the surface of a semiconductor and they might occur within the energy band gap [12]. These surface states are formed because of the termination of the solid that produces incomplete covalent bonds at the surface which, in turn, causes a change in the electronic band structure from bulk material to the vacuum [7]. New energy levels within the forbidden band gap of the semiconductor are created which can be either acceptor states or donor states and are characterised by a neutral level. The surface is electrically neutral if the surface states are occupied up to the neutral level and empty above that level (i.e. neutral one) [12]. When depositing metal on a semiconductor, the thermal equilibrium between metal and semiconductor occurs due to the occupation of the vacant states of the semiconductor atoms by some electrons from the valence band of the semiconductor surface. This process will lead to Fermi level pinning by the surface states. Consider a semiconductor with acceptor surface states whose density of states (D_s) is a constant over the energy range from the neutral level to the Fermi level, therefore, the negative surface state charge density is expressed by [3]

$$Q_{ss} = -qD_s(E_g - q\Phi_0 - q\Phi_{Bn} - q\Delta\Phi) \tag{3.39}$$

where Q_{ss} is the surface state charge density, Φ_0 is the energy levels at the surface and $\Delta\Phi$ is the Schottky barrier lowering. Please refer to Figure 3.1 for understanding the equation mentioned above.

3.6 Fermi level pinning

Fermi pinning is the phenomena that causes the Fermi level to be pinned due to the high density of interface states [13]. When a metal and semiconductor are brought into contact, thermal equilibrium will be attained, and the Fermi levels of the metal and semiconductor are aligned with each other

resulting in band bending in the semiconductor. The pinning of the Fermi level will result in the energy barrier heights being independent of the semiconductor work function [3]. The Schottky barrier height Φ_B and the built-in voltage V_s due to the surface states according to the Bardeen Model [14] are given by:

$$\Phi_B = (\Phi_m - \Phi_{SO}) + eV \tag{3.40}$$

$$V_s = [\frac{\Phi_m - \chi_s}{e}] + V_i \tag{3.41}$$

where Φ_{SO} and χ_S are the work function and electron affinity of the semiconductor, respectively, e is the electron charge and V_i is the voltage drop because of the surface states.

3.7 Barrier height inhomogeneities

The barrier height inhomogeneity effect comes from the variation of the barrier height across the interface area [15, 16]. Because of this effect, the current will preferentially flow through areas where the barriers are lower [15]. Assuming a Gaussian distribution of the inhomogeneous Schottky barrier height with a mean value $\bar{\Phi_B}$ and standard deviation σ_S, as described by [17, 18]

$$P(\Phi_B) = \frac{1}{\sigma_S\sqrt{2\pi}}\exp\left(-\frac{(\Phi_B - \bar{\Phi_B})^2}{2\sigma_S^2}\right) \tag{3.42}$$

where $\frac{1}{\sigma_S\sqrt{2\pi}}$ is the normalization constant of the Gaussian Schottky barrier height distribution. The following expression gives the total current $I(V)$ in the diode

$$I(V) = \int_{-\infty}^{+\infty} I(\Phi_B, V)P(\Phi_B)d\Phi. \tag{3.43}$$

By integrating Equation 3.43

$$I(V) = A^*AT^2\exp\left(-\frac{q\Phi_{\text{app}}}{kT}\right)\exp\left(\frac{qV}{n_{\text{ap}}kT}\right)\left[1-\exp\left(-\frac{qV}{kT}\right)\right] \tag{3.44}$$

with the saturation current I_s given by

$$A^{*}AT^{2}\exp\left(-\frac{q\Phi_{\text{app}}}{kT}\right) \tag{3.45}$$

where Φ_{app} and n_{ap} are respectively, the apparent Schottky barrier height and the ideality factor at a zero applied bias and they are expressed by

$$\Phi_{\text{app}} = \bar{\Phi}_{B(T=0)} - \frac{q\sigma_{S0}^{2}}{2kT} \tag{3.46}$$

and

$$\left[\frac{1}{n_{\text{app}}} - 1\right] = \rho_2 - \frac{q\rho_3}{2kT} \tag{3.47}$$

where $\bar{\Phi}_B$ is the mean Schottky barrier height, ρ_2 and ρ_3 the voltage coefficients which may depend on the temperature (T), and they quantify the voltage deformation of the Schottky barrier height distribution [19, 20]. Assuming that the mean value of the Schottky barrier height and the standard deviation are linearly bias-dependent on Gaussian parameters, for example $\bar{\Phi_B} = \bar{\Phi_{B0}} + \rho_{2V}$ and $\sigma_S = \sigma_{S0} + \rho_{3V}$. The extent of influence is determined by σ_S [21].

A plot of Φ_{app} versus $1000/T$ should yield a linear plot giving Φ_{B0} and σ_{S0}, respectively, from the intercept and the slope. Similarly, a plot of various values of the apparent ideality factor versus the temperature should be a straight line giving ρ_2 and ρ_3 respectively, from the intercept and the slope. Generally, the standard deviation is a measure of the barrier homogeneity. A lower value of σ_{S0} implies a homogeneous barrier height with good rectifying Schottky diode properties [21].

3.8 Cheung and Cheung method

SK Cheung and NM Cheung [22] developed a method for extracting the Schottky diode parameters such as n, Φ_B and R_s from single I-V measurements when the diodes deviate from the thermionic emission. A dimensionless quantity called the ideality factor n is usually involved in the I-V characteristic for the consideration of non-ideal diode behaviour. Also, the voltage drop across the diode V_D can be expressed in terms of the total voltage V across the total series resistance, and thus $V_D = V - IR$. The thermionic emission current given by Equation 3.3 can be written in terms of the current density $J = I/A$. Therefore, the applied voltage is given by [22]

$$V = R_s AJ + n\Phi_B + \frac{nkT}{q}\ln(J/A^{*}T^{2}). \tag{3.48}$$

By differentiating Equation 3.48 with respect to J we obtain

$$\frac{d(V)}{d(\ln J)} = RAJ + \frac{nkT}{q}. \tag{3.49}$$

Now by plotting $\frac{d(V)}{d(\ln J)}$ versus J, the slope of the linear portion will yield RA and the intercept with the y-axis will give $\frac{nkT}{q}$. In order to determine the Φ_B, a function $H(J)$ is defined as

$$H(J) = V - \frac{nkT}{q}\ln(J/A^*T^2). \tag{3.50}$$

By using Equation 3.48, Equation 3.50 can be reduced to

$$H(J) = RA + n\Phi_B \tag{3.51}$$

By plotting $H(J)$ versus J, the resulting straight line will have a slope RA and the y-axis intercept will yield $n\Phi_B$.

References

[1] S. S. Cohen, G. S. Gildenblat, Metal–semiconductor contacts and devices, 1^{st} Edn, Academic Press, 2014.

[2] Metal-Smiconductor Junction-Rectifying Contact; Available from, https://www.doitpoms.ac.uk/tlplib/semiconductors/junction_rectifying.php.

[3] S. M. Sze, K. K. Ng, Physics of semiconductor devices, 3^{rd} Edn, John wiley & sons, 2006.

[4] S. S. Li, Semiconductor physical electronics, 2^{nd} Edn, Springer Science & Business Media, 2012.

[5] L. J. Brillson, Y. Lu, ZnO Schottky barriers and Ohmic contacts, J. Appl. Phys. 109 (12) (2011) 8.

[6] W. Mtangi, Electrical characterization of process, annealing and irradiation induced defects in ZnO, Ph.D. thesis, University of Pretoria (2012).

[7] Metal-semiconductor contact; Available from, https://ecee.colorado.edu/~bart/book/book/chapter3/ch3_5.htm.

[8] S. M. Sze, K. K. Ng, Physics of semiconductor devices, 2^{nd} Edn, John wiley & sons, 1981.

[9] B. Sharma, Metal-semiconductor Schottky barrier junctions and their applications, Springer Science & Business Media, 2013.

[10] D. Schroder, Semiconductor material and device characterization, 3^{rd} Edn, John Wiley & Sons, 2006.

[11] W. R. Runyan, Semiconductor measurements and instrumentation, 2^{nd} Edn, McGraw-Hill, 1975.

[12] E. H. Rhoderick, Metal-semiconductor contacts,, IEE Proceedings I-Solid-State and Electron Devices 129 (1) (1982) 1.

[13] D. Song, B. Guo, Electrical properties and carrier transport mechanisms of n-ZnO/SiO_x/n-Si isotype heterojunctions with native or thermal oxide interlayers, J. Phys. D Appl. Phys. 42 (2) (2008) 025103.

[14] C. Malagù, M. C. Carotta, H. Fissan, V. Guidi, M. Kennedy, F. Kruis, G. Martinelli, T. Maffeis, G. Owen, S. Wilks, Surface state density decrease in nanostructured polycrystalline SnO_2: modelling and experimental evidence, Sensor. Actuat. B Chem. 100 (1-2) (2004) 283–286.

[15] Ş. Altındal, S. Karadeniz, N. Tuğluoğlu, A. Tataroğlu, The role of interface states and series resistance on the I–V and C–V characteristics in Al/SnO_2/p-Si Schottky diodes, Solid-State Electron. 47 (10) (2003) 1847–1854.

[16] R. Schmitsdorf, T. Kampen, W. Mönch, Correlation between barrier height and interface structure of AgSi (111) Schottky diodes, Surf. Sci. 324 (2-3) (1995) 249–256.

[17] S. Karadeniz, M. Şahin, N. Tuğluoğlu, H. Şafak, Temperature-dependent barrier characteristics of Ag/p-SnS Schottky barrier diodes, Semicond. Sci. Techn. 19 (9) (2004) 1098.

[18] J. H. Werner, H. H. Güttler, Barrier inhomogeneities at Schottky contacts, J. Appl. Phys. 69 (3) (1991) 1522–1533.

[19] A. Gümüş, A. Türüt, N. Yalcin, Temperature dependent barrier characteristics of CrNiCo alloy Schottky contacts on n-type molecular-beam epitaxy GaAs, J. Appl. Phys. 91 (1) (2002) 245–250.

[20] S. Acar, S. Karadeniz, N. Tuğluoğlu, A. Selcuk, M. Kasap, Gaussian distribution of inhomogeneous barrier height in Ag/p-Si (1 0 0) schottky barrier diodes, Appl. Surf. Sci. 233 (1-4) (2004) 373–381.

[21] C. Albert, Electrical and structural characterization of metal germanides, Ph.D. thesis, University of Pretoria (2010).

[22] S. Cheung, N. Cheung, Extraction of Schottky diode parameters from forward current-voltage characteristics, Appl. Phys. Lett. 49 (2) (1986) 85–87.

Chapter 4

Experimental procedure

4.1 Introduction

Undoped ZnO and (Ce, Sm and Al) doped and co-doped ZnO thin films were prepared from aqueous solutions using the sol-gel spin coating method. Similarly, the undoped ZnO nanorods and (Ce, Sm) doped and co-doped ZnO nanorods were fabricated using the low temperature CBD technique at 90° C. The thin films and the nanorods were grown on n-Si, ITO and microscope glass substrates. ZnO layers were first spin coated on the above-mentioned pre-cleaned substrates, followed by the growth of the nanorods using CBD. After that, samples were characterized in terms of the morphological, structural and optical properties, as will be discussed in more detail. Finally, contacts were fabricated on both thin films and nanorods prior to their electrical characterization.

4.1.1 Materials

Materials used for the synthesis of the ZnO thin films and nanorods were purchased and used as received without any further purifications, namely: zinc acetate $Zn(CH_3COO)_2.H_2O$ (98%, Merck), ethanol C_2H_5OH (98.4%), propan-2-ol C_3H_8O (98.99%, Merck), deionized (DI) water, zinc nitrate hexahydrate $Zn(NO_3)_2.6H_2O$ (98%, Sigma Aldrich), monoethanolamine (MEA) C_2H_7NO (98%, Merck), hexamethylenetetramine $C_6H_{12}N_{14}$ (99.5%, Sigma Aldrich), samarium nitrate hexahydrate $Sm(NO_3)_3.6H_2O$ (99.999%, Sigma Aldrich), cerium nitrate hexahydrate $Ce(NO_3)_3.6H_2O$ (99.999%, Sigma Aldrich) and aluminium nitrate nonahydrate $Al(NO_3)_3.9H_2O$ (99,997%, Sigma Aldrich).

4.1.2 Substrate cleaning

ITO glass substrates with dimensions of 20 mm $\times$ 10 mm $\times$ 2 mm and sheet resistance R_s of 12 Ω/sq were used. Glass and ITO substrates were cleaned with DI water, ethanol and acetone ultrasonically in

this order for 15 min each, and finally blown dry with nitrogen gas for the removal of any droplets that were left from the above-mentioned procedure. Si substrates with resistivity 1.4 - 1.8 Ω.cm, thickness of 380 μm and carrier concentration of 2.30 $\times 10^{15}$ cm^{-3} were used and cleaned using an ultrasonic bath with trichloroethlene, isopropanol, methanol and DI water in this order for 5 min each [1]. After that, Si substrates were etched by HF before evaporating the ohmic contact prior to the deposition of the films and nanorods. These cleaning procedures were followed for all samples used in this study.

4.1.3 Deposition of the ZnO thin films

A ZnO solution was prepared by dissolving an appropriate amount of zinc acetate dihydrate in a mixture of ethanol (60 ml) under continuous stirring at 500 rpm and 60° C(using a magnetic stirrer) for 1 hr. The MEA stabilizer was then added drop wise while continuously stirring for another 1 hr. The molar ratio of MEA:zinc acetate was kept at 1:1 throughout the experiment. The transparent, clear solutions were aged for a perioding (72 hrs to one week) to increase the gel viscosity. Aged ZnO solutions were then spin coated on pre-cleaned substrates (i.e. glass, ITO and n-Si) 5 times at 3000 rpm for 30 s (see Fig. 4.1 (a) and (b)). After each coating substrates with deposited films were dried in an oven at 150° C in air for 5 min to evaporate the solvents. Glass substrates with deposited films were annealed in a tube furnace at 500° C in air (1hr) while the n-Si substrates were annealed under flowing argon gas (30 min). Finally, deposited films were kept in a closed container for further characterization. Prior to nanorod deposition, the seeded substrates were dried at 150° in air for 10 min.

4.1.4 Deposition of Ce, Sm doped and co-doped ZnO thin films

The sol-gel solutions for the preparation of (Ce, Sm) doped and co-doped ZnO thin films were achieved by dissolving and adding appropriate amounts of dopants (0.25 M) to zinc acetate in 60 ml ethanol. First, Ce and Sm nitrate hexahydrate were dissolved separately and stirred at 3000 rpm at room temperature for 10 min and thereafter, solutions mixed together while continuing stirring for another 10 min. The solutions of Ce and Sm obtained were added to the zinc acetate and the resulting transparent solutions were aged for a period of 72 hrs to one week before use. Thereafter, the procedure for depositing the ZnO thin films described in 4.1.3 were then followed.

4.1.5 Ce and Al co-doped ZnO thin films

Ce and Al co-doped ZnO thin films were prepared using zinc acetate dihydrate, cerium nitrate hexahydrate, aluminium nitrate nonahydrate, isopropanol and MEA. Solutions for the preparation of Ce and Al co-doped ZnO thin films [$Zn_{1-x-y}Ce_xAl_yO$] were prepared by dissolving 1.0 at.% of Al and varying Ce concentrations (3.0, 5.0 and 7.0 at.%) separately in isopropanol (60 ml) while stirring

at 500 rpm at room temperature for 10 min. Finally, the solutions containing Al and Ce were mixed together and added to the zinc acetate solution, and the procedures for preparing ZnO films described in 4.1.3 were followed.

4.1.6 Fabrication of the ZnO nanorods

Synthesis of ZnO nanorods was achieved by dissolving equimolar amounts of zinc nitrate hexahydrate and HMTA (0.05 - 0.35 M) in DI water (200 ml) separately with continuous stirring for 10 min at room temperature, and finally mixing them together. The resulting milky solution was then placed in a hot water bath preheated to 90° C. Prior to the growth of the ZnO nanorods, the glass, ITO and Si substrates were first coated with ZnO seed layer as described in Section 4.1.3. Thereafter, seeded substrates were immersed into the solution of zinc nitrate and HTMA in such a way that the seeded sides of the substrates were facing downward. To avoid deposition of the nanorods on both sides of the substrates, the back side of the substrates were covered with a non-reactive, heat resistant tape. A schematic diagram showing seeded substrates before and after CBD deposition of the nanorods is depicted in Figure.4.1. Substrates with the vertically grown ZnO nanorods were thoroughly rinsed in DI water several times to remove any remaining residuals. Finally, substrates were blown dry with nitrogen gas and the samples were kept in closed containers for further characterization.

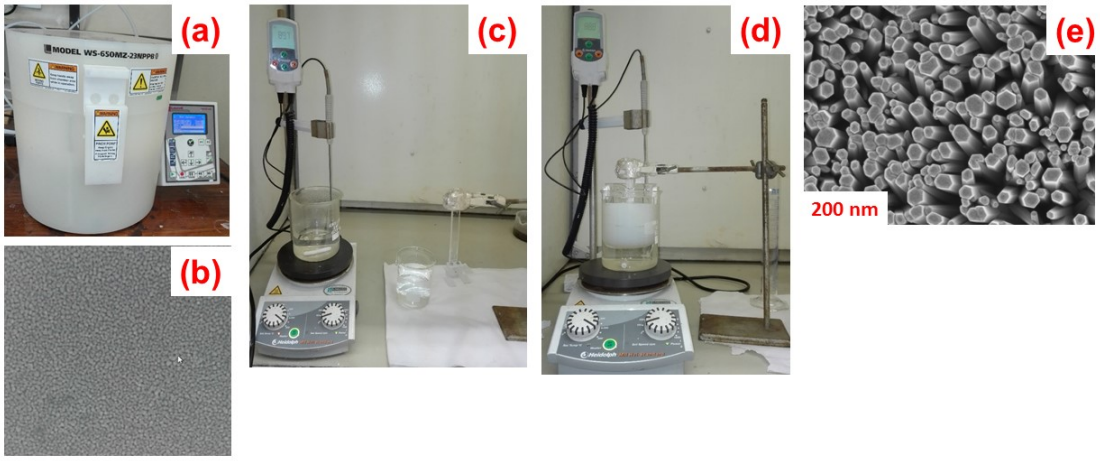

Fig. 4.1 Preparation of the ZnO thin films and nanorods using spin coating and CBD techniques, respectively. (a) Spin coater, (b) SEM image of the produced films after annealing, (c) preheated water at 90°C along side ZnO based solution and substrates with seeded side facing downward fixed to sample holder, (d) substrates immersed in the ZnO milky solution placed in a water bath and (e) SEM image of the CBD-grown ZnO nanorods.

4.1.7 Sm doped ZnO nanorods

Sm doped ZnO nanorods were fabricated on ITO substrates with undoped seeded ZnO thin films, using zinc nitrate hexahydrate, HMTA, samarium nitrate hexahydrate and DI water. Different concentrations of Sm (0.0, 1.5, 4.0 and 5.5 at.%) were dissolved separately in DI water and stirred at room temperature for 10 min and finally mixed together with the zinc nitrate solution and stirred for another 15 min to ensure that a homogeneous solution was obtained. Finally, the procedures for depositing ZnO nanorods were followed.

4.1.8 Ce doped ZnO nanorods

Ce doped ZnO nanorods were prepared using the same procedure described in 4.1.7 by varying the cerium nitrate concentration (0.0 ,4.0, 6.0, and 8.0 at.%). For the deposition of Ce doped ZnO nanorods, the procedures for growing ZnO nanorods in 4.1.6 were followed.

4.1.9 Ce and Sm co-doped ZnO nanorods

For the fabrication of Ce and Sm co-doped ZnO nanorods, samarium and cerium nitrate hexahydrate with different concentrations [$Zn_{1-x-y}Ce_xSm_yO$, $x+y$ = 0.0, 0.2, 0.4, 0.6, and 0.8 at.%, $x : y = 1 : 1$] were used. The dopants were separately dissolved in DI water and stirred for 15 min. Thereafter, Ce and Sm solutions were added to the mixture of zinc nitrate and HMTA and mixed thoroughly while stirring for another 10 min. Thereafter, the procedures that were used to fabricate ZnO nanorods described in 4.1.6 were followed.

4.2 Device fabrication

It is important in device fabrication to have good ohmic and rectifying contacts. In this study, ITO and AuSb (in the case of Si) were used as ohmic contacts. For rectifying contacts, Pd metal was employed for all samples. In the following subsection the procedures for depositing ohmic and Schottky contacts are outlined.

4.2.1 Ohmic and Schottky contacts

A 200 nm thick AuSb ohmic contact was deposited onto the unpolished side of the Si substrate using a resistive heating thermal evaporation system. After deposition, the Si substrates deposited with AuSb were annealed either in Ar or N atmosphere at a temperature 375° C for 10 min. In the case of ITO substrates, the un-deposited area of the ITO was used as an ohmic contact. For the Schottky contacts a 100 nm thick circular Pd contact, 0.6 mm in diameter was evaporated onto the top of the

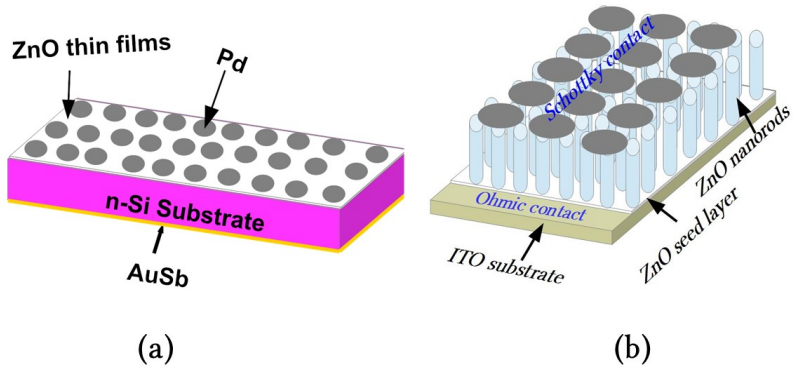

Fig. 4.2 Schematic diagram of deposited ohmic and Schottky contacts on (a) ZnO thin films on Si substrate and (b) ZnO nanorods on ITO substrate.

thin films and the nanorods using a resistive evaporator. A schematic diagram of the evaporated ohmic and Schottky contacts on ZnO thin films and nanorods is shown in Figure 4.2. The fabrication of the ohmic and Schottky contacts were done in a vacuum chamber at a pressure of 2.5×10^{-6} mbar and a deposition rate of 0.1 nm/s. Figure 4.3 depicts the thermal evaporation system.

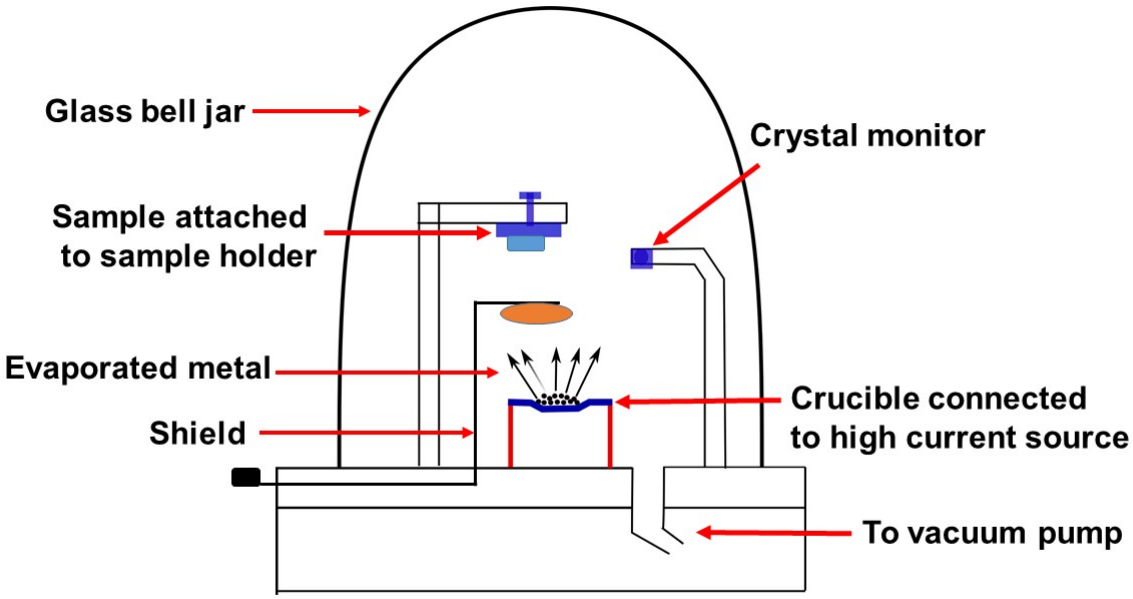

Fig. 4.3 Schematic diagram of the resistive evaporator.

4.3 Annealing furnace

The annealing for all samples was carried out using a heavy duty Lindberg furnace (200 °C to 1200 °C). The temperature of the furnace was controlled by a thermocouple placed underneath the sample holder. A schematic diagram of the annealing furnace used in this research is depicted in Figure. 4.4. The gases used as atmospheric annealing environment were nitrogen and argon in addition to air annealing.

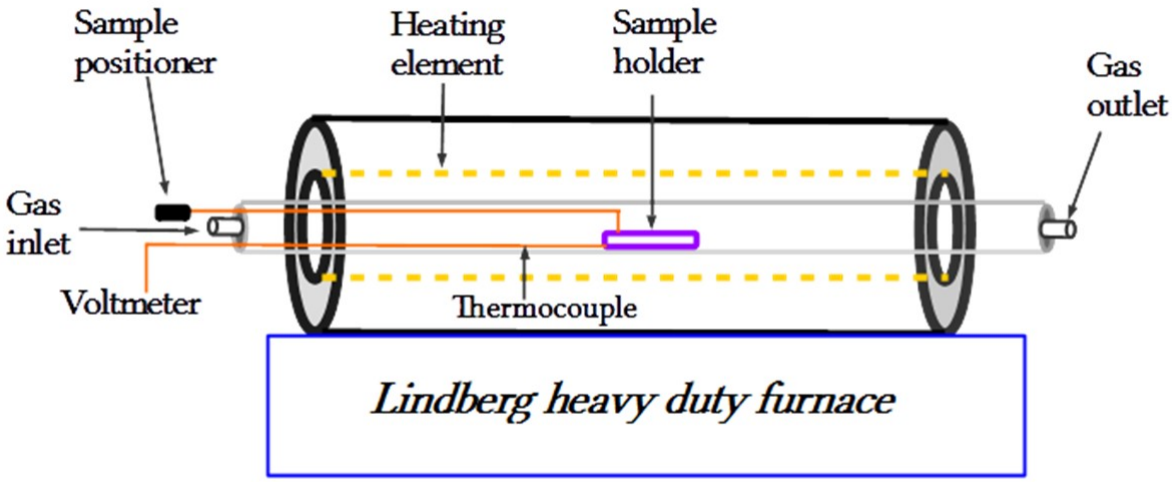

Fig. 4.4 Heavy duty *Lindberg* annealing furnace.

4.4 Characterization techniques

4.4.1 X-ray diffraction

X-ray diffraction (XRD) is a technique that is used to determine the phases present, degree of crystallinity, lattice parameters, orientation, stress, strain, composition as well as the grain size of the material under investigation [2]. The principle of XRD is the diffraction of waves by the periodic arrays of atoms [3]. Generally, x-rays are radiation with a short electromagnetic wavelength (0.7 - 2.3 Å) and high energy making the technique suitable for diffraction measurements in solid structures. When x-rays approach atoms they interfere and scatter because of the interaction between electrons in the atoms. This scattering produces a diffraction pattern with peaks at specific angles. These peaks are

directly related to the inter-atomic distances. When an x-ray beam with a certain wavelength λ hits the sample at an incident angle θ, constructive interference can occur according to Bragg's law [2]

$$n\lambda = 2d\sin\theta \tag{4.1}$$

where λ is the wavelength, n is an integer indicating the order of the diffraction peak, d represents the spacing distance between the planes of atoms and θ is the angle of the incident x-rays. By knowing the values of d, the crystal structure of the materials are then determined. For example, in case of a hexagonal crystal structure, the lattice parameters (i.e. $a = b$ and c) can be evaluated from [4, 5]:

$$\frac{c^2}{d^2} = \frac{4}{3}\left[\frac{h^2+k^2+hk}{a^2}\right]c^2 + l^2 \tag{4.2}$$

where h, k and l are the Miller indices, and the lattice parameters are denoted by a and c. The crystallite size D can also be calculated using [4]

$$D = \frac{0.9\lambda}{\beta_{hkl}\cos\theta} \tag{4.3}$$

where β and θ are the full width at half maximum (in radians) and the Bragg angle ($\theta = 2\theta/2$, in radians), respectively, and λ is the wavelength of the x-rays. In this study, the XRD data was collected using a Rigaku SmartLab X-Ray Diffractometer with Cu kα radiation and XPERT-PRO diffractometer in a $\theta/2\theta$ configuration, using a cobalt source tube at 35 kV, 50 mA and wavelength of 0.154 nm. A Bruker D8 Advance diffractometer supplied with copper anode operating at a voltage of 40 kV, current of 40 mA and wavelength of 0.154 nm was also used in this study.

4.4.2 Scanning electron microscopy

Scanning electron microscopy (SEM) is a technique that uses electrons to gain information from the surface of specimens,like the topography (texture) and the morphology of the samples (shape, surface, size and orientation of the particles). It uses electrons instead of the light to produce largely magnified images [6]. SEM can also be used to determine the chemical and elemental composition of the specimens using energy dispersive x-ray spectrometry (EDS) measurements.

The SEM technique relies on the principle that an accelerated electron beam from an electron gun interacts with the surface of the sample (see Figure 4.5). When the sample is bombarded with the focused and accelerated electron beam, different types of signals are produced from the sample surface, as shown in Figure 4.5. These signals include secondary electrons, diffracted and backscattered electrons, photons (used for elemental analysis), visible light and heat [6]. Secondary electrons are used to image the specimens surface (topography and morphology), while the backscattered electrons

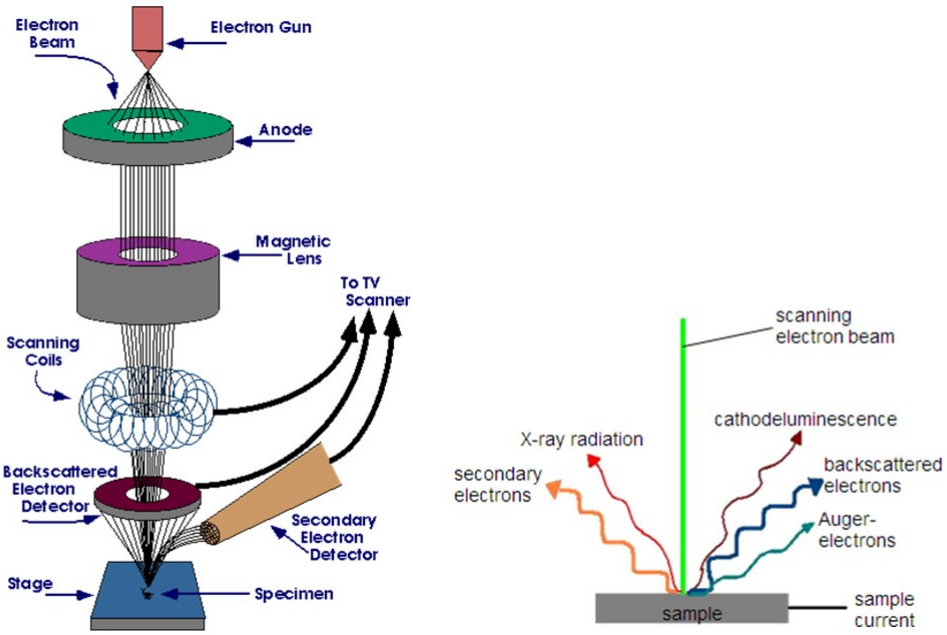

Fig. 4.5 Schematic diagram illustrating the scanning electron microscope system and different types of signals that can be produced during electron bombardment [6].

are used to determine the structure and the orientation of the specimens and also to provide contrast in multiphase samples. In this study, the surface morphology of all prepared samples were acquired by field emission scanning electron microscopy (FE-SEM ZEISS SEM-Microscope Crossbeam) using an in-lens detector utilized at a voltage of 1 kV. Prior to the measurements, all the samples were carbon coated to minimize surface charging. A schematic diagram of the SEM system is depicted in Figure 4.5.

4.4.3 X-ray photoelectron spectroscopy

X-ray photoelectron emission spectroscopy (XPS), also known as photoemission spectroscopy, is a technique that has been used intensively to study the chemical composition of solid materials [7–9]. The XPS technique is based on measurements of the kinetic energy of photoelectrons emitted from the sample after soft x-ray (1.5 kV) illumination in ultrahigh vacuum [5, 10]. When an atom is excited with an x-ray photon energy $h\nu$ from an initial state with energy E_i to a final state with energy E_f, an electron with kinetic energy E_k will be ejected and according to energy conservation [11]

$$E_k = h\nu - [E_f - E_i] - \Phi \tag{4.4}$$

where ν is the frequency of the x-ray, $E_f - E_i$ is the binding energy E_B of the state from which electrons is ejected and Φ is the work function (refer to Chapter 3). The binding energy E_B, which is roughly equal to the Hartree-Fock energy, is characteristic to the core electrons for a certain element and plays an important role in explaining the XPS spectra [5]. For a particular E_B the peak intensity is associated directly to the quantity of an element in the sample. The binding energy is also related to the oxidation state, i.e. E_B increases when the oxidation state increases. Thus XPS can provide information about the chemical composition as well as the oxidation state of the elements.

The XPS results presented in this study were obtained with a PHI 5000 scanning ESCA Microprobe. A 100 μm diameter monochromatic AlK_α x-ray beam with $h\nu = 1486.6$ eV was used to analyze the different binding energies. A low energy Ar^+ ion gun and neutralizer electron gun were used to minimize the surface charging. The overall energy resolution for all spectra was set to 0.5 eV. Multipack software version 9.0 was used to analyze the spectra and to identify the electronic states of the elements using Gaussian-Lorentzian fits.

4.4.4 Raman spectroscopy

Raman spectroscopy is known as a non-destructive technique used to investigate the materials' vibrational modes, as well as the orientation. The Raman technique is based on inelastic scattering of a small fraction $\approx 10^{-7}$ of the electromagnetic radiation by the molecules of the material under investigation [2]. When material is illuminated by an incident monochromatic light, the majority of the light will be scattered elastically (without a change in wavelength), but a minority will be scattered inelastically (Raman effects). The shift in the wavelength depends on the chemical structure of the molecules accountable for the scattering [12]. The Raman scattered light may be separated according to wavelength using a grating and is then detected by a charge-coupled detector (CCD). Raman spectra are obtained when the material is irradiated with a laser source of (visible or near-infrared) monochromatic radiation, followed by measuring, recording and displaying the scattered radiation using a suitable spectrometer [13].

By using the frequencies of the incident and scattered Raman light, the vibrational energy difference (Raman shifts) can be calculated. The Raman shift is expressed in the Raman spectrum as wavenumbers (cm^{-1}) [2]. The Raman spectra for all samples in this thesis were acquired using a Jobin Yvon, Horiba TX64000. The laser source used has an excitation wavelength of 514 nm and a power of 0.012 W. For the samples focusing, LWX50 and LWX100 microscope objectives were used interchangeably. A WITec alpha 300R confocal Raman spectroscope (for high resolution confocal Raman imaging) was also used in this study using a laser with excitation wavelength of 530 nm.

4.4.5 Ultraviolet-visible spectroscopy

Ultraviolet-visible spectroscopy (UV-vis) is a technique based on the measurement of light absorption by electronic transitions in the material under study. These electronic transitions require wavelengths typically in the UV-visible region of the electromagnetic spectrum [5]. When light of intensity I_0 passes through a transparent material, different process can occur. These include transmittance, absorption and reflection of the light by the sample. The transmittance (T) of light through a transparent materials is defined as the ratio of the transmitted light intensity (I) to the incident light intensity I_0 [5],

$$T = \frac{I}{I_0} \tag{4.5}$$

The absorbance (A) is defined

$$A = \log\left[\frac{I_0}{I}\right] = \varepsilon lc = \alpha c \tag{4.6}$$

where ε is the molar absorptivity (measure of how well the material absorbs a certain wavelength of light), l is the thickness of the sample, c represents the sample concentration and α is the absorption coefficient. The value A can be determined from the experimentally measured values of I_0 and I. The absorption coefficient is wavelength dependent and a plot of α versus wavelength λ is the absorption spectrum [5]. This spectrum is a a property of a measured sample and therefore it reflects the fundamental electronic properties of the sample.

The main components of the instrument are a source, a monochromator and a detector. The sources for UV and visible/near infrared region measurements are a deuterium lamp (190 - 350 nm) and a halogen/tungsten lamp (350-900), respectively. Before measuring the transmittance of the samples, baseline correction was done by placing a pre-cleaned blank substrate (ITO and/or glass) with coated side facing the light sources. After that, samples deposited on ITO or glass substrates were placed in one of the sample holders (coated side facing the light source) while keeping the reference in the other holder. The transmittance measurements were preformed in the wavelength range 200 to 800 nm. In this study, a Varian Cary 100 UV-vis and a Lambda 950 UV-vis spectrometer were used to study the optical transmittance in the wavelength range from UV (200 - 400 nm) to visible light (400 - 800 nm). A schematic diagram of the UV-vis instrument is shown in Figure 4.6.

4.4.6 Photoluminescence spectroscopy

Photoluminescence (PL) spectroscopy is a technique that measures the excitation and emission of luminescent materials. The principle of PL is very similar to that of UV-vis spectroscopy. They both

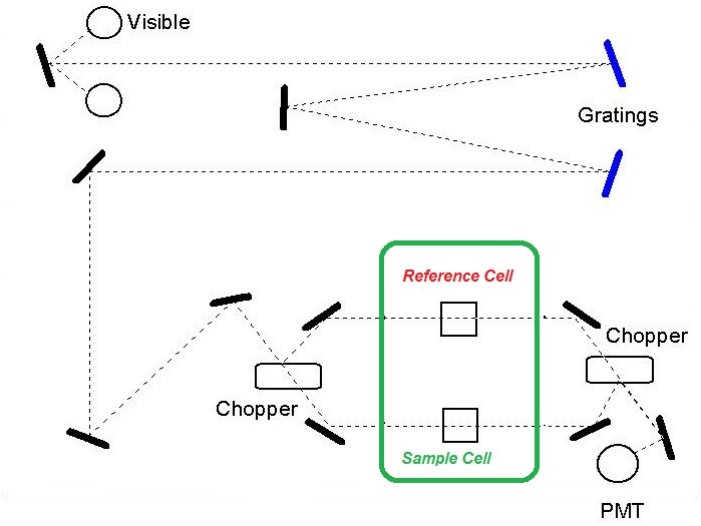

Fig. 4.6 Schematic diagram of the UV-vis spectrometer [14].

require an electronic transition from initial to final states, however, the main difference is that the transition in the PL is from higher to lower energy levels. Also, no signal is detected from the sample if there is no PL, unlike the absorption spectroscopy which is a non-zero background experiment [5]. A typical PL spectrum is a plot of the PL intensity as a function of the wavelength measured at a fixed value of excitation wavelength [5].

Figure 4.7 depicts the key components of a typical PL spectrofluorometer. When the source generates photons, they enter a monochromator that only transmits an excitation wavelength used to excite the sample. The emitted light from the sample is directed by lenses, distributed by another monochromator and thereafter detected by a detector (e.g CCD, photodiode or PMT). The generated electrical signal from the detector is then converted to a digital signal using an analog to digital convertor and finally processed on a computer using software [5]. In this study, PL data were obtained using a Cary Eclipse fluorescence spectrophotometer with He-Cd laser (325 nm) PL system. The Cary Eclipse is supplied with a xenon lamp (200 - 1100 nm) used for a wide spectrum of excitation wavelengths and PMT detector.

4.4.7 Current-voltage and capacitance-voltage characteristics

The current-voltage (*I-V*) measurement is a technique for examining the behaviour and the quality of the Schottky diodes. From the *I-V* curve under both forward and reverse bias, it is easy to know if the deposited Schottky contact is a good rectifier or is an ohmic contact. From the analysis of the *I-V* characteristics, information regarding the diode properties can be obtained, such as the ideality factor n, Schottky barrier height Φ_B, series resistance R_s and the saturation current I_s, as well as the dominant transport mechanism in the diode.

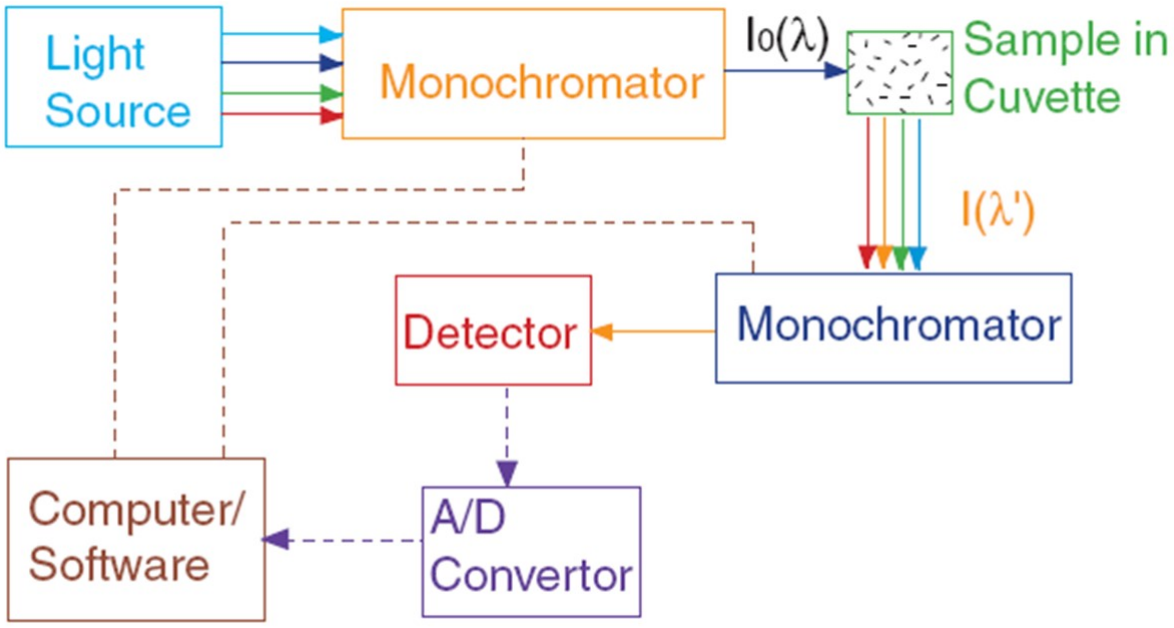

Fig. 4.7 Schematic representation of the basic component of the PL spectrofluorometer. Adapted from Ref [5].

Capacitance-voltage (*C*-*V*) measurements are also used to determine the diode quality and extracting some parameters such as the barrier height and the built-in voltage. From the *C*-*V* depth profile one can also obtain the net doping density of the semiconductor. Measurements of the *I*-*V* and *C*-*V* characteristics were performed in the dark at room temperature. Typically, the measurement system comprises of a probe station and HP 4140B pA Meter/DC Voltage Source with current sensitivity down to 10^{-12} A. An HP 4192A LF Impedance analyser was used for the *C*-*V* measurements of the contact. A schematic digram of the *I*-*V* and *C*-*V* station is depicted in Figure. 4.8.

References

[1] A. Farag, W. Farooq, F. Yakuphanoglu, Characterization and performance of Schottky diode based on wide band gap semiconductor ZnO using a low-cost and simplified sol–gel spin coating technique, Microelectron. Eng. 88 (9) (2011) 2894–2899.

[2] Y. Leng, Materials characterization: introduction to microscopic and spectroscopic methods, John Wiley & Sons, 2009.

[3] X-ray powder diffraction (XRD), https://serc.carleton.edu/research_education/geochemsheets/techniques/XRD.html.

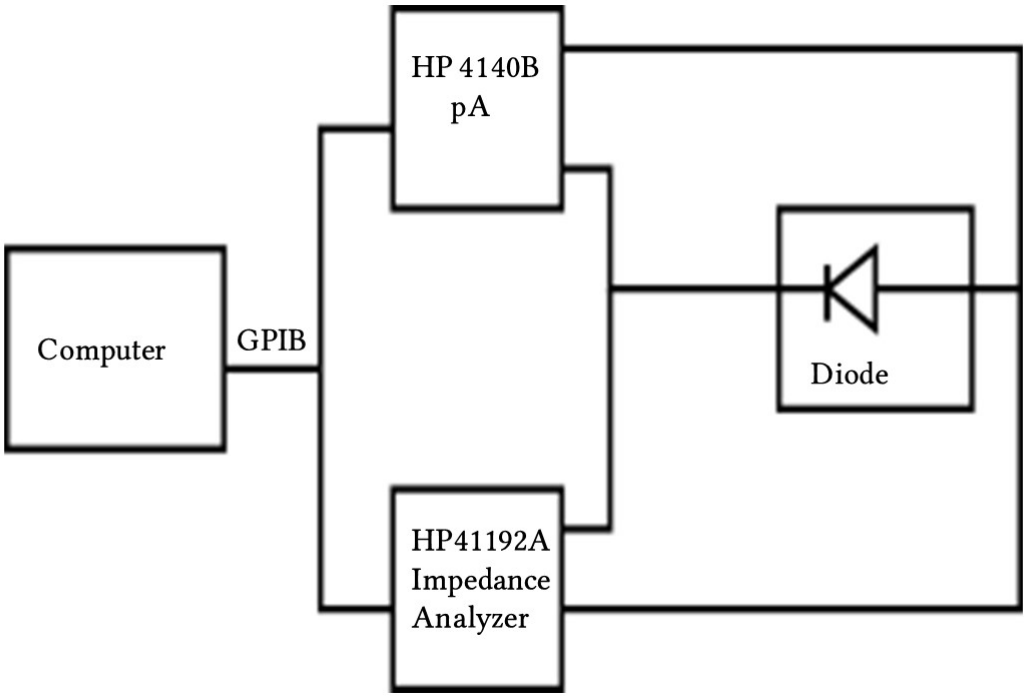

Fig. 4.8 Schematic diagram of the *I-V*, *C-V* measurement station.

[4] N. Sinha, G. Ray, S. Bhandari, S. Godara, B. Kumar, Synthesis and enhanced properties of cerium doped ZnO nanorods, Ceram. Int. 40 (8) (2014) 12337–12342.

[5] Z. J. Zhong, Optical properties and spectroscopy of nanomaterials, World Scientific, 2009.

[6] Scanning Electron Microscopy;available from, https://www.purdue.edu/ehps/rem/laboratory/equipment%20safety/Research%20Equipment/sem.html.

[7] C. S. Fadley, Angle-resolved x-ray photoelectron spectroscopy, Prog. Surf. Sci. 16 (3) (1984) 275–388.

[8] M. Chen, X. Wang, Y. Yu, Z. Pei, X. Bai, C. Sun, R. Huang, L. Wen, X-ray photoelectron spectroscopy and auger electron spectroscopy studies of Al-doped ZnO films, Appl. Surf. Sci. 158 (1-2) (2000) 134–140.

[9] D. Yang, A. Velamakanni, G. Bozoklu, S. Park, M. Stoller, R. D. Piner, S. Stankovich, I. Jung, D. A. Field, C. A. Ventrice Jr, et al., Chemical analysis of graphene oxide films after heat and chemical treatments by X-ray photoelectron and Micro-Raman spectroscopy, Carbon 47 (1) (2009) 145–152.

[10] T. Barr, Modern ESCA The Principles and Practice of X-Ray Photoelectron Spectroscopy, 1st Edn, CRC press, 1994.

References

[11] S. Hüfner, Photoelectron spectroscopy: principles and applications, 3^{rd} Edn, Springer,Berlin, 2003.

[12] D. A. Skoog, F. J. Holler, S. R. Crouch, Principles of instrumental analysis, 6^{th} Edn, Thomson, 1970.

[13] I. R. M. Ramos, A. Malkin, F. Lyng, Current advances in the application of Raman spectroscopy for molecular diagnosis of cervical cancer, BioMed Res. Int. 2015.

[14] Varian Cary 100; Available from, https://people.stfx.ca/tsmithpa/chem362/labs/VarianCary.html.

Chapter 5

Results and discussion: part 1

5.1 Structural, optical and electrical properties of Ce doped ZnO thin films prepared via wet chemical technique

5.1.1 Introduction

This section presents the results published on the Schottky diode fabricated on undoped ZnO and RE (Ce, Sm) doped and co-doped ZnO thin films. The films were prepared using sol-gel spin coating technique [1, 2]. The undoped and doped ZnO films were spin-coated (four layers) on pre-cleaned glass slides and n-Si substrates for optical and electrical characterization, respectively. The resulting films were annealed at 500° C and characterized by XRD, FESEM and EDS respectively, for the structural, surface morphology and elemental composition. Moreover, PL and UV-vis studies were carried out for the optical properties. Furthermore, the *I-V* characteristics of the fabricated Schottky diode devices Pd/ZnO/n-Si/AuSb (on undoped, (Ce, Sm) doped and co-doped ZnO thin films) were used for the electrical characterization.

5.1.2 Results and discussion

XRD results of the obtained films revealed their polycrystalline nature with the main peaks corresponding to (100), (002) and (101). XRD also showed the absence of Ce, Sm and their oxides in the XRD pattern. It is also found that the lattice parameters for the Sm doped ZnO and Ce doped ZnO increased compared to the undoped one. However, for the Sm and Ce co-doped ZnO the lattice parameters were found decrease. This increase in the lattice parameters could be due to the successful substitution of a larger ionic radius of the dopant, while the decrease in the case co-doping may be attributed to the distortion in the ZnO lattice due to the larger ionic radius of the Sm and Ce together. Figure 5.1 (A) presents the SEM images of undoped ZnO, and (Ce, Sm) doped and co-doped ZnO thin

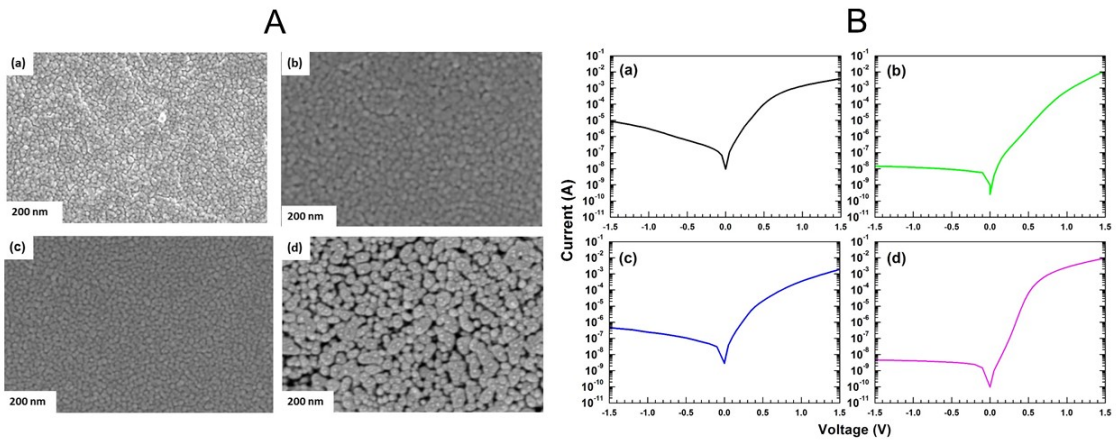

Fig. 5.1 (A) SEM images and (B) the *I-V* characteristics of the fabricated Schottky diode devices: (a) undoped, (b) Sm-doped, (C) Ce-doped and (d) Ce and Sm co-doped ZnO films.

films. SEM images of the deposited films showed uniform films with a particle size in the range 9.70 to 22.7 nm. EDS results revealed the presence Ce and Sm elements alongside Zn and O, indicating that Ce and Sm were incorporated into the ZnO lattice [3].

PL studies of all films showed a UV and very weak blue emission located at 370 nm and no deep level (defect) emission. The disappearance of the defect emission in the annealed films indicate that annealing removed the defects from the samples [4]. It is also observed that the intensity of the UV peak is not strong and sharp as expected. This could also be attributed to the effect of the post annealing. The optical band gap measured from the transmittance spectra using Tauc plots for undoped ZnO, Sm-doped ZnO, Ce-doped ZnO, Ce and Sm co-doped ZnO were 3.22, 3.20, 3.20 and 3.10 eV, respectively.

The semilogarithmic *I-V* characteristics of the fabricated Schottky diode devices Pd/ZnO/n-Si/AuSb Schottky diodes based on undoped, Ce and Sm doped and co-doped ZnO thin films are shown in Figure 5.1 (B). The contacts were fabricated as described in the experimental chapter. As can be seen, the structures demonstrated good rectification behaviour. The maximum rectification order achieved is six orders magnitude with (Ce and Sm) co-doped ZnO films compared to undoped ZnO, which is two orders of magnitude. A good rectification indicated that good ohmic and Schottky contacts were fabricated. A summary of the fabricated Schottky diode properties is given in Table 5.1. As can be observed both ideality factor and series resistance decreased after co-doping compared to undoped ZnO, Ce and Sm doped.

Table 5.1 Schottky barrier height, ideality factor, saturation current and series resistance of Pd/ZnO/n^+ - Si/AuSb Schottky diodes.

Samples	Φ_{B0} (eV)	n	I_s (A)	$R_s(\Omega)$
undoped ZnO	0.66	2.84	1.14×10^{-7}	612
Sm-doped ZnO	0.76	2.83	4.15×10^{-8}	29
Ce-doped ZnO	0.70	2.63	2.67×10^{-8}	52
Ce/Sm-co-doped ZnO	0.82	1.62	2.77×10^{-10}	60

The transport mechanism in the fabricated Schottky diode devices at low voltages is controlled by an ohmic behaviour; however, at higher voltages, the generation recombination process and space charge-limited current was also observed. From the above-motioned results, it is concluded that both Ce and Sm doped and co-doped ZnO thin films have improved the Schottky diode properties of the thin films compared to undoped ZnO.

More information on the effect of doping and co-doping of ZnO thin films on the structural, optical and electrical properties are given in the published article in Material Research Bulletin.

Publication I: Structural, optical and electrical properties of the fabricated Schottky diodes based on ZnO, Ce and Sm doped ZnO thin films prepared via wet chemical technique

5.2 Effect of (Ce, Al) co-doping of ZnO on its structural, optical and electrical properties

5.2.1 Introduction

The results obtained from the undoped ZnO and (Ce, Al) co-doped ZnO films of [$Zn_{1-x-y}Ce_xAl_yO$, ($x = 3.0$, 5.0 and 7.0 at.% and $y = 1$ at.%)] synthesized using wet chemical sol-gel spin coating technique are discussed in this section. The films were spin-coated on microscope glass and on n-Si substrates. The Schottky and ohmic contacts were Pd (100 nm) and AuSb (200 nm), respectively. All films were characterized by FESEM, XRD and Raman spectroscopy. The optical studies were done using PL and UV-vis spectroscopy. Finally, the electrical properties of the fabricated Schottky diodes were studied using *I-V* characteristics. All films were characterized at room temperature.

5.2.2 Results and discussions

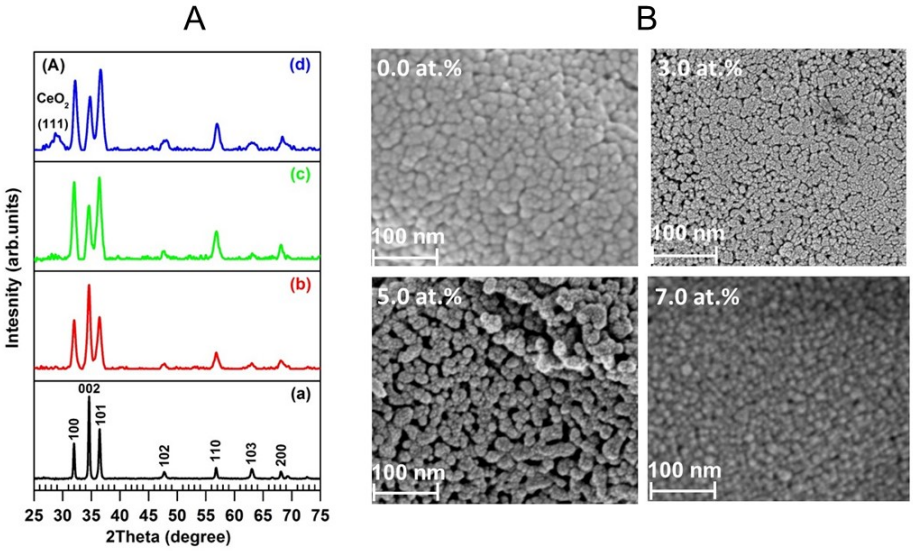

Fig. 5.2 (A) and (B) are the XRD pattern and SEM images of the undoped ZnO and (Ce, Al) co-doped ZnO films: (a) 0.0, (b) 3.0, (c) 5.0 and (d) is 7.0 at.%.

XRD patterns of the $Zn_{1-x-y}Ce_xAl_y$ are shown in Figure 5.2 (A). XRD results showed that all films were polycrystalline with prominent peaks corresponding to (100), (002) and (101). XRD also revealed that at lower dopant concentrations, the dopants have been incorporated successfully into the ZnO lattice, as confirmed by the absence of peaks related to Al, Ce or their oxides. At the higher level of doping (7.0 at.%) cerium dioxide peaks were detected indicating that the Ce has exceeded the

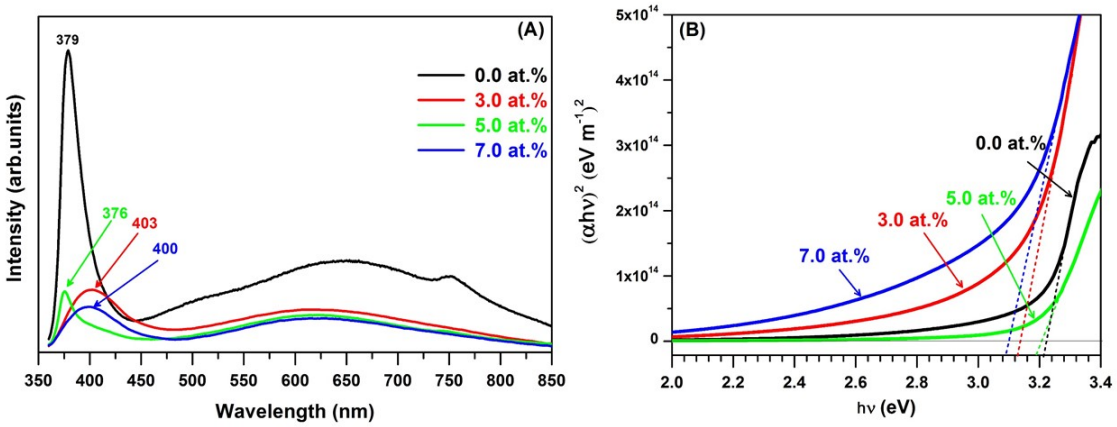

Fig. 5.3 (A) and (B) is PL spectra and (B) the Tauc plots of the undoped ZnO and (Ce, Al) co-doped ZnO thin films at (0.0, 3.0, 5.0 and 7.0) at.% Ce and 1.0 at.% Al.

solubility limit. Due to Ce and Al co-doping, the main peaks (100), (002) and (101) showed a small shift which indicated that the successful incorporation of the dopants into the ZnO lattice caused a small change in the lattice parameter. Figure 5.2 (B) shows the FESEM images of the undoped ZnO and (Ce, Al) co-doped ZnO films. Uniform films were obtained with particle sizes found in the range 10.0 nm to 30 nm and film thicknesses in the 900 nm to 1.3 μm range.

The phonon vibration studies of all films revealed several vibrational modes located at 278, 333, 439, 464, 580 and 1100 cm^{-1}. Raman studies also revealed that the E_2 high mode located at 439 cm^{-1} was the dominant peak and the appearance of the peak at 464 alongside the E_2 high peak in the 7.0 at.% sample was assigned to cerium dioxides.

Figure 5.3 (A) shows the PL spectra of the undoped ZnO films and (Ce, Al) co-doped ZnO films. PL showed two emission peaks, namely, near band edge emission (NBE) and deep level emission. The UV emission intensities decreased with increasing dopant concentration, and the position of the UV peak was red-shifted compared with undoped ZnO films. The undoped ZnO films showed deep-level emission (green-orange) in the 450 - 850 nm range centred at 640 nm. However, after doping the emission peak shifted from 640 nm (red emission) to 615 nm (orange emission) and the intensity was found to decrease upon increasing the doping concentration (see Figure 5.3 (A)). The optical band gap determined from the transmittance spectra using a Tauc's plot for the undoped ZnO and (Ce, Al) co-doped ZnO at Ce concentrations 0.0, 3.0, 5.0 and 7.0 at% were 3.22 eV, 3.13 eV, 3.20 eV and 3.10 eV, respectively.

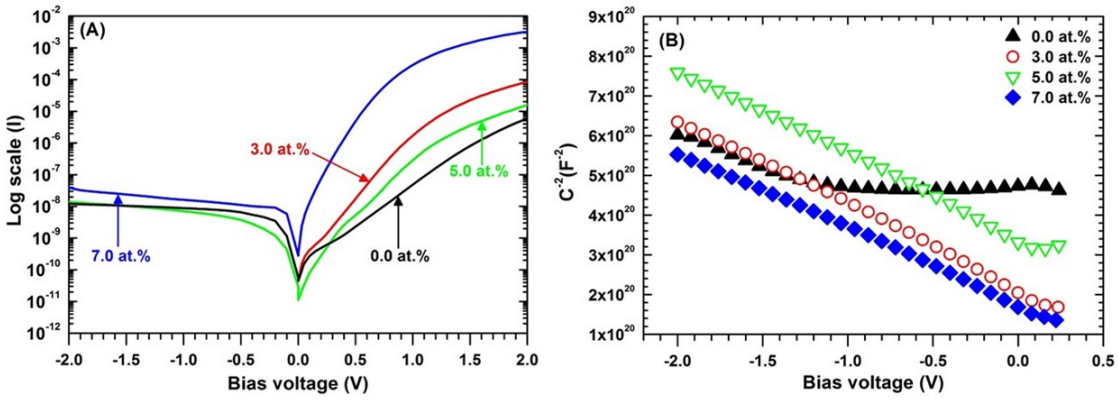

Fig. 5.4 (A) represent the *I-V* and (B) the *C-V* characteristics of the fabricated Schottky diode devices with 0.0, 3.0, 5.0 and is 7.0 at.% Ce and 1.0 at.% Al.

Figure 5.4 (A) depicts the *I-V* characteristics of the Pd/ZnO/n-Si/AuSb Schottky diodes for the undoped ZnO and (Ce, Al) co-doped ZnO thin films. The structures exhibited good rectification behaviour which improved upon doping with a maximum rectification ratio at 2.0 V (five orders of magnitude) obtained at higher levels of doping. A summary of the fabricated Schottky diode properties extracted using the thermionic emission theory (neglecting the effect of the series resistance) are presented in Table 5.2. The ideality factors of all fabricated Schottky diodes were considerably higher than the ideal value (i.e. 1). This could be attributed to factors such as voltage drop across the metal-semiconductor junction, interface states, barrier height inhomogeneity and series resistance [5, 6]. It can be seen from Table 5.2 that the best device obtained with maximum doping (i.e 7.0 at.% Ce), where the formation of CeO_2 is observed. The presence CeO_2 could be responsible for the improvements in the diode properties. By taking into account the effect of the series resistance the values of the Schottky diode properties will differ from those obtained using conventional thermionic emission theory. Thus, the ideality factors, Schottky barrier height and the series resistance were determined using the Cheung method [7] and the results are also tabulated in Table 5.2.

Figure 5.4 (B) shows the C^2-*V* characteristics of the Schottky diodes based on undoped and (Ce, Al) co-doped ZnO thin films. The extracted values of the free electron carrier concentrations from C^2-*V* are presented in Table 5.2. The barrier height from the C^2-*V* was found to be 1.70 eV, 2.85 eV, 1.35 eV and 1.18 eV, respectively. These values are higher compared to those obtained from *I-V* measurements. Furthermore, the free-electron carrier concentrations were found to decrease after doping compared to the undoped ZnO.

Table 5.2 Schottky diode parameters evaluated using conventional ln I vs. V and Cheung method and carrier concentration from C-V depth profiles for undoped and (Ce, Al) co-doped ZnO thin films.

$Zn_{1-x-y}Ce_xAl_yO$	ln$I$ vs. V			$d(V)/d(\ln I)$			$H(I)$			N_{dcv}
	n	$\Phi_{B_0}(eV)$	$R_s(\Omega)$	n	$\Phi_{B_0}(eV)$	$R_s(\Omega)$	n	$\Phi_{B_{eff}}(eV)$	$R_s(\Omega)$	cm^{-3}
x=0.00,y=0.00	4.97	0.76	42k	7.98	-	81	-	0.74	81.87k	1.7×10^{17}
x=0.03,y=0.01	3.84	0.84	5k	6.98	-	4.29k	-	0.77	5.77k	2.1×10^{16}
x=0.05,y=0.01	2.64	0.83	33k	7.58	-	22k	-	0.80	28	1.2×10^{16}
x=0.07,y=0.01	2.40	0.77	262	5.27	-	243	-	1.46	258	1.0×10^{16}

An article published in Material Science in Semiconductor Processing gives details on the effect of the (Ce, Al) co-doping ZnO thin films on the Schottky diode properties.

Publication II: Effect of (Ce, Al) co-doped ZnO thin films on the Schottky diode properties fabricated using the sol-gel spin coating

References

[1] Z. Xu, H. Deng, Y. Li, Q. Guo, Y. Li, Characteristics of Al-doped c-axis orientation ZnO thin films prepared by the sol–gel method, Mater. Res. Bull. 41 (2) (2006) 354–358.

[2] M. Ahmed, S. Mwankemwa, E. Carleschi, B. Doyle, W. Meyer, J. Nel, Effect of Sm doping ZnO nanorods on structural optical and electrical properties of Schottky diodes prepared by chemical bath deposition, Mater. Sci. Semicond. Process. 79 (2018) 53–60.

[3] M. Ahmed, W. Meyer, J. Nel, Structural, optical and electrical properties of the fabricated schottky diodes based on ZnO, Ce and Sm doped ZnO films prepared via wet chemical technique, Mater. Res. Bull. 115 (2019) 12–18.

[4] M. Wang, K. Lee, S. H. Hahn, E. J. Kim, S. Kim, J. S. Chung, E. W. Shin, C. Park, Optical and photoluminescent properties of sol-gel Al-doped ZnO thin films, Mater. Lett. 61 (4-5) (2007) 1118–1121.

[5] L. J. Brillson, Y. Lu, ZnO Schottky barriers and ohmic contacts, J. Appl. Phys. 109 (12) (2011) 8.

[6] N. S. Singh, L. Kumar, A. Kumar, S. Vaisakh, S. D. Singh, K. Sisodiya, S. Srivastava, M. Kansal, S. Rawat, T. A. Singh, et al., Fabrication of zinc oxide/polyaniline (ZnO/PANI) heterojunction and its characterisation at room temperature, Mater. Sci. Semicond. Process. 60 (2017) 29–33.

[7] S. Cheung, N. Cheung, Extraction of Schottky diode parameters from forward current-voltage characteristics, Appl. Phys. Lett. 49 (2) (1986) 85–87.

Chapter 6

Results and discussion: part 2

6.1 Introduction

In this chapter, the effect of Ce and Sm doping and co-doping on ZnO nanorods grown using a two-step CBD technique are discussed. All the fabricated ZnO nanorods based on undoped ZnO, Ce and Sm doped and co-doped ZnO were characterized at room temperature in terms of their structural, morphological and phonon vibration by XRD, FESEM and Raman spectroscopy, respectively. The elemental composition was determined using XPS and EDS. The optical properties of the nanorods were studied with UV-vis and PL spectroscopy. Finally, the electrical properties of the fabricated Schottky diodes were studied using *I-V* characteristics.

The results discussed are presented in three sections. In Section 6.2, the effect of Sm doping of ZnO nanorods on the properties of the Schottky diode is discussed. The effect of doping ZnO nanorods with Ce at different concentration levels on the structural, optical and electrical properties are presented in section 6.3. Finally, in section 6.4, the influence of (Ce, Sm) co-doping of ZnO nanorods on the structural, optical and electrical properties are explained in detail.

6.2 Effect of Sm doping of ZnO nanorods on structural, optical and electrical properties of Schottky diodes prepared by chemical bath deposition

6.2.1 Results and discussions

Figure 6.1 (A) shows the XRD patterns of the undoped and Sm-doped ZnO nanorods at concentrations 0.0, 1.5, 4.0, and 5.5 at.%Sm. XRD revealed that the as-synthesized ZnO nanorods were highly crystalline with preferential growth along the (002) reflection plane. It was found that the Sm dopants

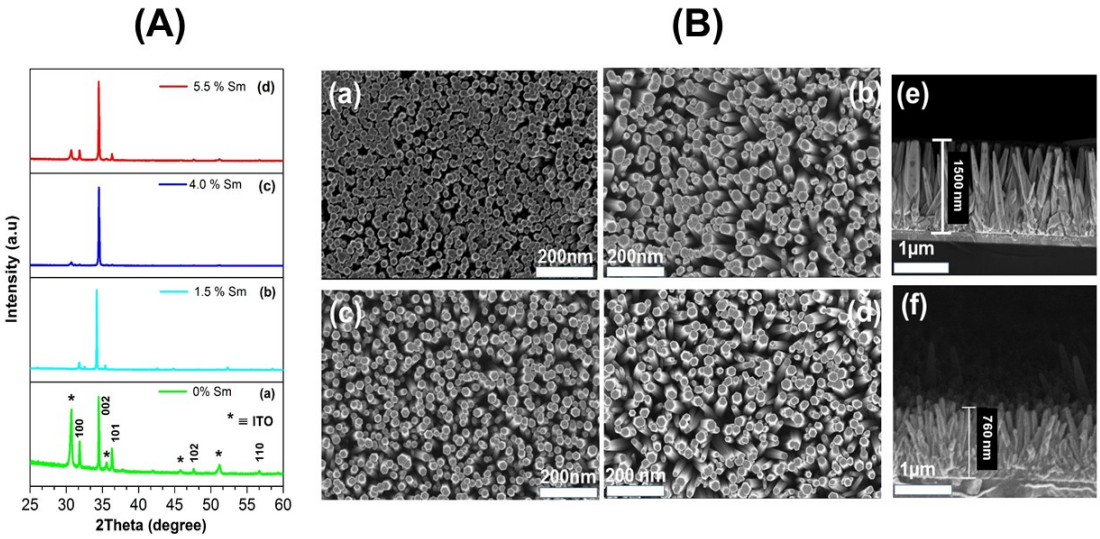

Fig. 6.1 (A) and (B) are the XRD and SEM images of as-synthesized ZnO samples. (a) 0.0, (b) 1.5, (c) 4.0, (d) 5.5 at.% Sm. The length of the undoped ZnO nanorods and 5.5 at.% Sm-doped ZnO nanorods are depicted in (e) 1500 nm and (d) 761 nm, respectively.

were successfully incorporated into the ZnO lattice. The incorporation of Sm was confirmed by the absence of Sm elements and its oxides peaks, and also by the small shift in the (002) peak. Due to the difference in the ionic radius between the Sm^{3+} (0.096 nm) and Zn^{2+} (0.074 nm), the lattice constant was found to decrease after doping compared to the undoped ZnO nanorods. SEM images shown in Figure 6.1 revealed that ZnO maintains its hexagonal structure up to the maximum doping used and that the growth of the nanorods was affected by Sm doping. The Raman studies of as-synthesized ZnO nanorods showed that the E_2 high peak appeared to be sharp and dominant over the vibrational modes, indicating that samples were of highly crystalline, as supported by XRD results.

PL spectra of the undoped and Sm-doped ZnO nanorods are shown in Figure 6.2. Two PL emission peaks were observed in the spectra, namely, strong UV located around 400 nm and a broad emission in the 480 - 670 nm range. A weak peak around 750 nm was also observed for all samples. The UV emission peak, which is due to the free exciton recombination process was found to red-shift at higher levels of doping compared to the undoped ZnO [1, 2]. The green-yellow emission peak, as reported in the literature, is caused by the oxygen vacancies, donor-acceptor transitions [3], zinc vacancies and surface defects [4, 5]. The intensity of the green-yellow emission after Sm doping (4.0 and 5.5 at.%) was found to decrease, which could be due to crystal defects present in the samples. Figure 6.2 center and right shows the *I-V* characteristics of the Pd/n-ZnO/ITO Schottky diodes based on undoped and Sm doped ZnO nanorods. The structure exhibited a rectification behaviour for undoped ZnO and Sm-doped ZnO at 1.5 at.% with ideality factors respectively, of 4.8 and 2.5. However, for

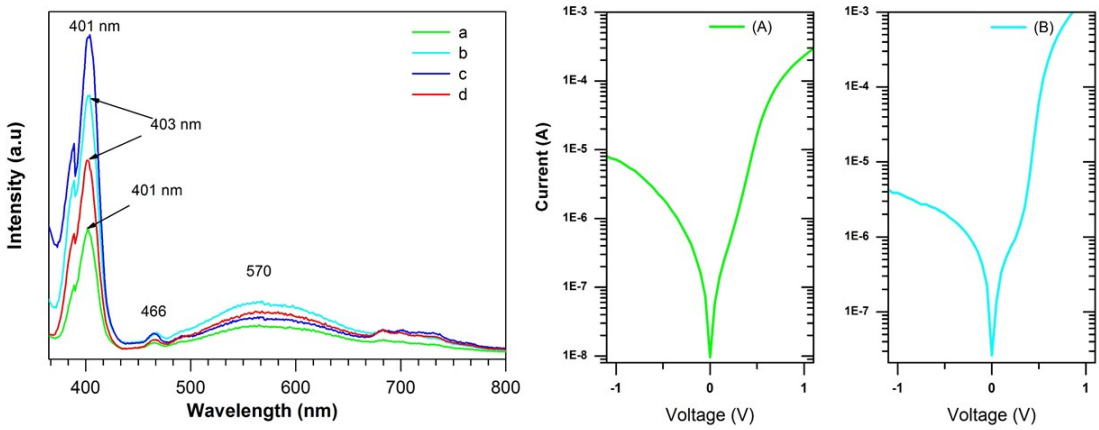

Fig. 6.2 (Left) PL spectra of undoped and Sm-doped ZnO nanorods (a) 0.0, (b) 1.5, (c) 4.0 and (d) is 5.5 at.%. (Right) Semilogarithmic *I-V* characteristics of undoped ZnO nanorods (A) and 1.5 at.% Sm-doped ZnO.

Sm-doped at 4.0 and 5.5 at.%, no rectification behaviour was observed, which could be attributed to the Sm doping, but probably more likely to be the formation of poor Schottky contacts.

More information on the effect of Sm doping of ZnO nanorods on the Schottky diode properties can be found in the following article.

Publication III: Effect of Sm doping ZnO nanorods on structural, optical and electrical properties of Schottky diodes prepared by chemical bath deposition

6.3 Structural, optical and electrical properties of a Schottky diode fabricated on Ce doped ZnO nanorods grown using a two step chemical bath deposition

6.3.1 Results and discussions

XRD results showed that the as-synthesized samples based on undoped and Ce (0.0, 2.0, 4.0, 6.0 and 8.0 at.%) doped ZnO nanorods were grown along the reflection plane (002). The XRD pattern revealed that the as-synthesized samples had good crystalline quality with no other phases related to cerium or cerium oxides. Results from XRD also revealed that the cerium dopant successfully incorporated into the ZnO lattice. Moreover, due to the higher ionic radius of Ce^{3+} and Ce^{4+} (1.03 Åand 0.92 Å) compared to the Zn^{2+} (0.74 Å), the (002) peaks was shifted toward higher 2θ values.

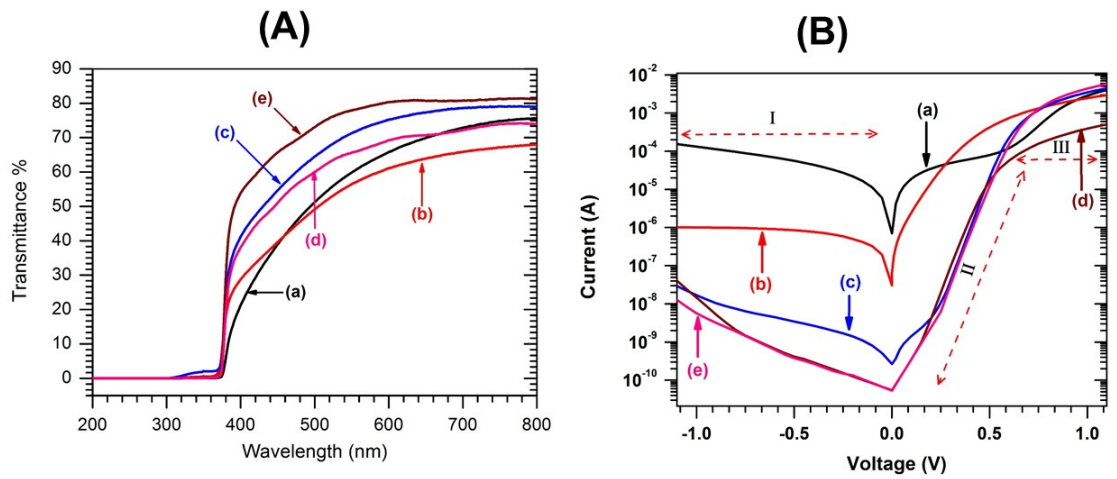

Fig. 6.3 (A) UV-Vis transmittance spectra and (B) *I-V* characteristics of the Pd/ZnO/ITO based on undoped and Ce doped ZnO nanorods. (a) 0.0, (b) 2.0, (c) 4.0, (d) 6.0 and (e) is 8.0 at.% Ce doping.

Figure 6.3 (A) shows the transmittance spectra of the undoped and Ce-doped ZnO nanorods. The optical band gap extracted from Tauc plots for Ce doping at 0.0, 2.0, 4.0, 6.0 and 8.0 at.% was found to be 3.24 eV, 3.24 eV, 3.27 eV, 3.29 eV and 3.29 eV, respectively. This increase in the optical band gap for the Ce-doped ZnO compared with the undoped material could be attributed to the well know Moss-Burstein phenomenon [6–8]. Figure 6.3 (B) depicts the *I-V* characteristics of the Schottky diodes fabricated on pure and Ce-doped ZnO nanorods. The structure manifested an excellent rectification behaviour after doping of ZnO with Ce. Schottky diode parameters obtained from the fit using conventional thermionic emission theory are presented in Table 6.1. Interestingly,

Table 6.1 Schottky diodes parameters obtained from the *I-V* characteristics, barrier height, ideality factor, saturation current and the series resistance.

Concentration (at%)	ϕ_B (eV)	n	I_s (Amps)	$R_s(\Omega)$
0.0	0.553	4.45	79.13×10^{-8}	112
4.0	0.764	3.00	12.64×10^{-11}	144
6.0	0.826	1.36	9.10×10^{-12}	126
8.0	0.824	1.37	23.12×10^{-12}	1034
10.0	0.856	1.34	3.43×10^{-12}	80

the ideality factor was found to decrease with increasing Ce contents. However, the series resistance increased after Ce doping, except for Ce at 10.0 at.%, in which it showed a decrease compared to undoped ZnO. The increase in the series resistance could be caused by a formation of a bad contact between the Pd and the nanorods, possibly due to the presence of an oxide layer within the interface.

The following article published in Materials Science in Semiconductor Processing gives detailed information about the effect of doping ZnO nanorods with Ce on the structural, optical and electrical properties.

Publication IV: Structural, optical and electrical properties of a Schottky diode fabricated on Ce doped ZnO nanorods grown using a two step chemical bath deposition

6.4 Influence of co-doping with Ce and Sm on the ZnO nanorods on the structural, optical and electrical properties of Schottky diodes using chemical bath deposition

6.4.1 Results and discussions

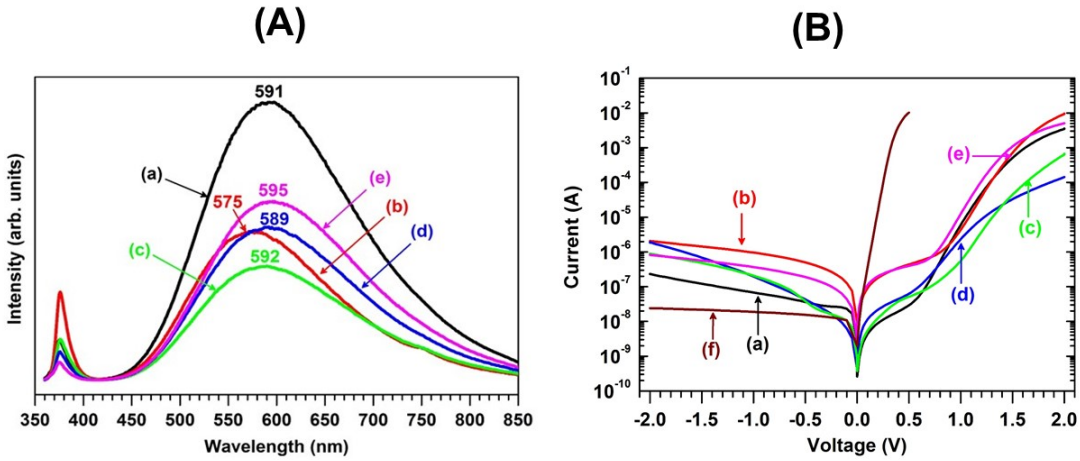

Fig. 6.4 (A) PL spectra and (B) is *I-V* characteristics of the Schottky diode devices. (a) 0.0, (b) 0.2, (c) 0.4, (d) 0.6 and (e) is 0.8 at.% doping. (f) shows the *I-V* characteristics of the structure Pd/n-Si/AuSb.

XRD revealed that the as-grown ZnO nanorods based on pure and (Ce, Sm) co-doped ZnO nanorods at total concentration of Ce and Sm (0.0, 0.2, 0.4, 0.6 and 0.8 at.% and a Ce:Sm ratio of 1:1) were grown preferentially along the (002) direction. XRD also showed that the intensity of the dominant (002) peak increased after doping, indicating the improvement of the crystalline quality. No other peaks related to Ce, Sm and their oxides were observed in the XRD, which confirmed the successful incorporation of the dopants into the ZnO lattice.

Figure 6.4 (A) shows the PL spectra of the as-synthesized ZnO nanorods based on the undoped and (Ce, Sm) co-doped material. Two emission peaks were observed in the PL spectra, namely, weak UV emission around 378 nm and strong deep-level emission in the 450 - 850 nm range. The maximum emission was obtained with the undoped ZnO nanorods, which may be ascribed to intrinsic defects that are strongly dependent on the synthesis process. To identify the multiple bands that contributed to the deep-level emission in all samples, deconvolution of the peak was carried out to all spectra using Gaussian fits. The deconvoluted spectra revealed that more than one defect contributed to the

deep-level emission. Furthermore, the deep-level emission intensity first decreased after doping up to 0.4 at.%, and thereafter, it increased again at higher levels of doping.

The electrical characterization of the Pd/ZnO/n-Si/AuSb Schottky diodes revealed good rectification behaviour (see Figure 6.4 (B)). After Ce and Sm co-doping the rectification order was found to decrease compared to the undoped ZnO nanorods. The ideality factor and the series resistance responded to the (Ce, Sm) co-doping and were found to decrease. Moreover, it was also found from the *I-V* characteristics that, the generation recombination process in the fabricated device increased with increasing dopant concentrations. A summary of the fabricated Schottky diode device parameters extracted from the *I-V* characteristics using conventional thermionic emission theory are presented in Table 6.2.

Table 6.2 Ideality factor (n), Schottky barrier height (Φ_B), series resistance (R_s), saturation current (I_s) and valence band offset (ΔE_v) of the fabricated Schottky diode based on undoped and (Ce, Sm) co-doped ZnO nanorods.

Ce and Sm at.%	n	Φ_B (eV)	R_s Ω	I_s (A)	ΔE_v (eV)
0.0	3.32	0.784	103	44.5×10^{-12}	1.83
0.2	3.88	0.745	26	206.3×10^{-12}	1.58
0.4	5.11	0.704	2.17k	1.03×10^{-9}	1.81
0.6	4.57	0.758	215.6	122×10^{-12}	1.83
0.8	3.70	0.734	95	315.4×10^{-12}	1.85
n-Si	1.06	0.750	12	8.24×10^{-9}	$--$

The following article gives detailed information on the structural, optical and electrical properties of the (Ce, Sm) co-doping of ZnO nanorods.

Publication V: Influence (Ce, Sm) co-doping ZnO nanorods on the structural, optical and electrical properties of the fabricated Schottky diode using chemical bath deposition

References

[1] M. H. Huang, Y. Wu, H. Feick, N. Tran, E. Weber, P. Yang, Catalytic growth of zinc oxide nanowires by vapor transport, Adv. Mater. 13 (2) (2001) 113–116.

[2] Y. Kong, D. Yu, B. Zhang, W. Fang, S. Feng, Ultraviolet-emitting ZnO nanowires synthesized by a physical vapor deposition approach, Appl. Phys. Lett. 78 (4) (2001) 407–409.

[3] Y. Wang, S. Lau, X. Zhang, H. Lee, S. Yu, B. Tay, H. Hng, Evolution of visible luminescence in ZnO by thermal oxidation of zinc films, Chem. Phys. Lett. 375 (1-2) (2003) 113–118.

[4] A. B. Djurišić, W. C. Choy, V. A. L. Roy, Y. H. Leung, C. Kwong, K. W. Cheah, T. Gundu, W. K. Chan, H. Fei, C. Surya, Photoluminescence and electron paramagnetic resonance of ZnO tetrapod structures, Adv. Funct. Mater. 14 (9) (2004) 856–864.

[5] Y. Heo, D. Norton, S. Pearton, Origin of green luminescence in ZnO thin film grown by molecular-beam epitaxy, J. Appl. Phys. 98 (7) (2005) 073502.

[6] C. Wu, J. Shen, J. Ma, S. Wang, Z. Zhang, X. Yang, Electrical and optical properties of molybdenum-doped ZnO transparent conductive thin films prepared by dc reactive magnetron sputtering, Semicond. Sci. Techol. 24 (12) (2009) 125012.

[7] V. Kumari, V. Kumar, B. P. Malik, R. M. Mehra, D. Mohan, Nonlinear optical properties of erbium doped zinc oxide (EZO) thin films, Opt. Commun. 285 (8) (2012) 2182–2188.

[8] P. F. H. Inbaraj, J. J. Prince, Optical and structural properties of Mg doped ZnO thin films by chemical bath deposition method, J. Mater. Sci. Mater. Electron. 29 (2) (2018) 935–943.

Chapter 7

Concluding remarks and future work

7.1 Conclusion

This study aimed to synthesize and characterize new materials that can be used in optoelectronic devices based on Ce, Sm and Al doped and co-doped ZnO thin films and nanorods using low-temperature sol-gel and chemical bath deposition methods, respectively. Samples were deposited on pre-cleaned ITO coated glass substrates and n-Si substrates.

In Section 5.1 the fabrication and characterization of Ce and Sm doped and co-doped ZnO thin films were reported. Successfully fabricated Pd/ZnO/n-Si/AuSb Schottky diodes based on undoped and (Ce, Sm) doped and co-doped ZnO thin films using the low-cost sol-gel spin coating technique. XRD results revealed that all grown samples were polycrystalline with the absence of impurity phases, indicating the successful incorporation of the dopant into the ZnO lattice. PL spectra showed that the UV emission consisted of two peaks located at 388 nm and 405 nm, and the absence of deep-level emission. UV-vis transmittance revealed that the optical band gap decreased when the dopants were introduced. Maximum transmittance (83 %) was obtained with Sm-doped ZnO. The room temperature *I-V* characteristics of the fabricated Schottky diodes manifested excellent devices for the Ce and Sm co-doped ZnO with the lowest ideality factor (1.62) and series resistance of 60 Ω. Furthermore, three different transport mechanisms were observed in our Schottky diodes; namely, the tunnelling, recombination and space charge limited current.

Section 5.2 describes the synthesis and characterization of Pd/ZnO/n-Si/AuSb Schottky diodes based on undoped and (Ce, Al) co-doped ZnO thin films produced by sol-gel spin coating. XRD results showed that particle size and the lattice parameters decreased upon increasing the levels of doping; however, the FWHM increased with increasing doping concentration up to lower doping concentration (5.0 at.%), indicating that the dopants incorporated into the ZnO lattice. XRD revealed a cerium dioxide peak at a higher doping concentration (7.0 at.%), indicating that the cerium dopant exceeded the solubility limit. Raman spectroscopy confirmed the wurtzite structure of ZnO by the

presence of a sharp and intense E_2 high mode. Raman studies also confirmed the presence of cerium dioxide at maximum levels of doping. PL spectra showed two peaks, UV and broad deep-level emission, and that the intensity of both peaks decreased after doping. Maximum transmission of uv-visible-near infrared radiation was obtained ($\sim 72\%$) with 5.0 at.% Ce and 1.0 at.% Al-doped ZnO films. The *I-V* characteristics of all films revealed a rectification behaviour with a maximum (nearly five orders of magnitude) obtained with 7.0 at% Ce and 1.0 at.% Al. A barrier height of 0.77 eV, ideality factor of 2.40 and series resistance of 262 Ω were obtained for these samples. Analysis of the electrical properties according to the method of Cheung resulted in values that were higher compared with those obtained using conventional thermionic emission theory. Furthermore, the free-electron carrier concentration was found to be lower for the doped samples compared to the undoped ZnO thin films.

Chapter 6 reports on the fabrication and characterization of (Ce, Sm) doped and co-doped ZnO nanorods. In section 6.2, undoped and Sm doped ZnO nanorods were successfully synthesized on seeded ITO glass substrates using the CBD method. The XRD results revealed that Sm^{3+} ions have been incorporated successfully into the ZnO lattice with no impurities or other phases detected. Raman spectra showed the as-grown nanorods were highly crystalline by the presence of an intense, sharp E_2 (high) peak. The UV-vis transmittance revealed a decrease in the optical band gap after Sm doping. The PL spectra showed a strong UV emission and broad deep-level emission peak (green-yellow) in the visible region. The presence of a strong UV emission peak indicated the high crystal quality of the as-grown nanorods. The deep-level emission peak intensities were enhanced upon increasing the Sm concentration, indicating more defects were introduced, which agreed well with Raman scattering results. The XPS results revealed the presence of Zn and O with a small amount of C used for calibration and Sm in the 5.5 at.% Sm doped ZnO. Moreover, the XPS analysis showed the presence of oxygen vacancies within the undoped and Sm-doped ZnO nanorods. The *I-V* characteristics showed rectifying behaviour of Schottky diodes which was improved by two orders of magnitude when ZnO nanorods were doped with Sm at 1.5 at.%.

In section 6.3, Schottky diodes based on undoped and Ce-doped ZnO nanorods were grown on ITO substrates using the CBD technique. XRD results revealed that the as-synthesized nanorods were highly crystalline and grown perpendicularly to the ITO substrate. The absence of Ce related XRD peaks and other impurities indicated the successful incorporation of Ce into the ZnO lattice. Raman spectra presented an intense, sharp E_2 (high) mode peak, also indicating highly crystalline ZnO nanorods were grown. The E_2 (high) mode peak was red-shifted when increasing the Ce dopant concentrations. The PL spectra showed two peaks, namely, UV and green-yellow (deep-level) emission peaks. PL also showed enhancement of the green-yellow emission after Ce doping. UV-vis spectroscopy revealed an increase in the optical band gap after Ce doping. The electrical properties of the fabricated Schottky diodes were determined from *I-V* characteristics. The Schottky diode rectification behaviour was improved by increasing the Ce concentration with maximum rectification obtained at 10.0 at% Ce, having an ideality factor and barrier height of 1.34 and 0.856 eV, respectively.

In section 6.4 undoped and (Ce, Sm) co-doped ZnO nanorods grown on n-Si substrates using CBD assisted with a low-cost sol-gel spin coated seed layer. FESEM images revealed that the ZnO had maintained its hexagonal structure up to higher levels of doping. XRD results showed that the as-synthesized nanorods were highly crystalline and grown along the c-axis, as expected, and no peaks related to Ce and Sm or their oxides were found. Raman spectroscopy results revealed that the prominent E_2 (high) mode shifted toward a lower wavenumber and that the intensity decreased after doping. The XPS results showed the expected spectra associated with Zn and O, and the presence of Ce and Sm were observed at higher doping (0.8 at.%). The analysis of high-resolution spectra revealed the presence of oxygen vacancies in all samples. PL spectra showed a weak UV emission peak and strong deep-level emission peak. The intensity of the deep-level emission first decreased upon doping, up to 0.4 at.%, and then enhanced again at higher concentrations. Results from the deconvolution of the deep-level emission spectra showed that more than one defect contributed to the visible emission. The *I-V* characteristics of the fabricated Schottky diode devices revealed a rectification behaviour. The ideality factor decreased with increasing doping concentrations. Results from *I-V* characteristics also indicated that the co-doping had increased the generation-recombination process in the device. Furthermore, the current transport mechanism at lower voltages (up to ~ 0.6 V) was dominated by the ohmic conduction transport mechanism while at a higher voltage (above $\sim$ 0.6 V), the space charge-limited current and the trap filled limit voltage were the dominant transport mechanisms.

From this study we can conclude that both Ce and Sm doped and co-doped ZnO thin films and nanorods can be used for the fabrication of Schottky diode devices.

7.2 Future Work

For future work it is good to investigate the electrical properties for both thin films and nanorods using deep-level transient spectroscopy (DLTS). The study of the effect of alpha particle and proton irradiation on the properties of the Schottky diodes using DLTS. Growing these sample on a highly doped n-Si might minimize the series resistance and therefore improve the diode quality.